

Summer 8-2017

Effect of Boundary-Layer Tripping on Turbulence Generation and Trailing-Edge Noise in Transitional Airfoils

James Benjamin Lewis
Embry-Riddle Aeronautical University

Follow this and additional works at: <https://commons.erau.edu/edt>



Part of the [Aerodynamics and Fluid Mechanics Commons](#)

Scholarly Commons Citation

Lewis, James Benjamin, "Effect of Boundary-Layer Tripping on Turbulence Generation and Trailing-Edge Noise in Transitional Airfoils" (2017). *Doctoral Dissertations and Master's Theses*. 370.
<https://commons.erau.edu/edt/370>

This Thesis - Open Access is brought to you for free and open access by Scholarly Commons. It has been accepted for inclusion in Doctoral Dissertations and Master's Theses by an authorized administrator of Scholarly Commons. For more information, please contact commons@erau.edu.

EFFECT OF BOUNDARY-LAYER TRIPPING ON TURBULENCE GENERATION
AND TRAILING-EDGE NOISE IN TRANSITIONAL AIRFOILS

A Thesis

Submitted to the Faculty

of

Embry-Riddle Aeronautical University

by

James Benjamin Lewis

In Partial Fulfillment of the

Requirements for the Degree

of

Master of Science in Aerospace Engineering

August 2017

Embry-Riddle Aeronautical University

Daytona Beach, Florida

EFFECT OF BOUNDARY-LAYER TRIPPING ON TURBULENCE GENERATION
AND TRAILING-EDGE NOISE IN TRANSITIONAL AIRFOILS

by

James Benjamin Lewis

A Thesis prepared under the direction of the candidate's committee chairman, Dr. Reda Mankbadi, Department of Aerospace Engineering, and has been approved by the members of the thesis committee. It was submitted to the School of Graduate Studies and Research and was accepted in partial fulfillment of the requirements for the degree of Master of Science in Aerospace Engineering.

THESIS COMMITTEE



Chairman, Dr. Reda Mankbadi



Member, Dr. Vladimir Golubev



Member, Dr. Anastasios Lyrintzis



Graduate Program Coordinator, Dr. Magdy Attia

8.22.2017

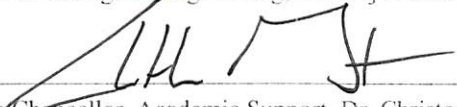
Date



Dean of College of Engineering, Dr. Maj Mirmirani

8/22/2017

Date



Vice Chancellor, Academic Support, Dr. Christopher Grant

8/23/2017

Date

ACKNOWLEDGMENTS

I am humbled, and honored to have been a part of this work. To be selected by the United States Air Force right out of my undergraduate study at Ohio State, accepted into the prestigious Scientist & Engineer's Palace Acquire Program, and granted entry into Embry-Riddle Aeronautical University's Masters of Aerospace Engineering program, it has been an excellent series of events in my life. It has culminated into the biggest professional challenge of my life to date. Presently, I have had the distinct privilege to be led by my thesis advisor, Dr. Reda Mankbadi, which I have regarded every day to be a great honor. It is with great esteem, and sincere respect that I express appreciation for his efforts to guide me in studying the arts of aerodynamics, and aeroacoustics, while keeping my mathematics skills sharp. Additionally, I would like to thank Dr. Vladimir Golubev, and Dr. Anastasios Lyrintzis for having served on my committee. Their expert observations and superb feedback throughout this process has broadened my education and helped me immensely.

To my colleagues and friends in our group, Dr. Lap Nguyen and Mr. Saman Salehian, I would also like to extend sincere gratitude. Their endless patience, support, and expert training has continuously expanded my skillset, and will benefit me for years to come.

Cooperative assistance with Dr. Dan Garmann of the AFRL, WPAFB, Dr. Chris Bahr of NASA Langley Research Center, Virginia, and Dr. Michaela Herr of DLR, Germany must also be recognized. Dr. Garmann assisted in the understanding of the inner-workings of the code FDL3DI and how best to leverage it, as well as how to employ pressure-probe data acquisitions, and some FORTRAN post-processing techniques. Dr.

Herr provided mentorship and encouragement through correspondence, also sharing expertise, knowledge, and data. Dr. Bahr showed comradery in sharing expertise, knowledge, in addition to providing guidance and assistance in the development of several post-processing acoustic scripts.

To Dr. Greg Brooks, and Mr. Mark Jurkovich for their expert advice on interfacing with Linux, and the HPC. To Mr. Andrew Fields for his skilled coding in MATLAB. To Mr. Ron Buhrman for his patience and communication in teaching me to speak, and interpret FORTRAN. To Melissa Rapiere for her guidance in the PAQ program. To my Branch Chiefs over the past two years who have shown me endless support. To the USAF, and the HPC, thank you.

To my wife, who without her none of this is possible, for her patience, support, and loyalty. To my children for bringing extraordinary joy into my life, granting me perspective, and continuing to test my patience. Praise be to God for being the foundation of my life.

TABLE OF CONTENTS

LIST OF TABLES	vi
LIST OF FIGURES	vii
SYMBOLS.....	x
ABBREVIATIONS	xi
ABSTRACT.....	xii
1. Introduction	1
1.1. Background Information	1
1.2. Motivation	2
1.3. Sources of Noise.....	2
1.4. Previous Work.....	5
2. Computational Methodologies	9
3. Two-Dimensional Results	11
3.1 Grid and Boundary Conditions	11
3.2 Preliminary Verifications	15
3.3 Effect of Location on Tripping	19
.....	25
4. Three Dimensional Results	32
4.1 Grid and Boundary Conditions	32
4.2 Snap shots of the flow & acoustic field tripping vs. clean.....	34
4.3 The Sound Sources.....	39
4.3.1 Flow over the Airfoil Surface	39
4.3.2 Spectral Analysis	46
4.3.3 Trailing-Edge and the Wake Flow.....	51
4.4 The Acoustic Field	61
5. Conclusions	67
REFERENCES	69

LIST OF TABLES

Table 3.1: Case 1 simulation matrix for the BANC Workshop (Herr et al., 2015).	13
Table 3.2: Parametric grid study varying trip location.	20
Table 3.3: One-third octave bands standardized [Engineering Toolbox.com].	29
Table 4.1: NACA-0012 grids employed in 3D studies.	34
Table 4.2: Normalization values per case for Figure 4.27.	63

LIST OF FIGURES

Figure 1.1 Airfoil self-noise mechanisms, with relevant mechanisms outlined (Brooks et al., 1989).	4
Figure 1.2 Tonal noise regimes of a NACA 0012 associated with VS (Paterson, 1973).. ..	7
Figure 3.1 Baseline 2D grid far field to $r=100$ chord (top), to near field displaying extensive mesh refinement (bottom).....	12
Figure 3.2 Coefficient of Drag (top), Coefficient of Lift (middle), and Moment Coefficient (bottom) vs. non-dimensional time for the baseline case of an untripped NACA 0012 airfoil.	14
Figure 3.3 Chord-wise distribution of the time-averaged mean surface pressure coefficient, $C_p (x/l_c)$	17
Figure 3.4 Location of flow field data acquisition.....	18
Figure 3.5 U-velocity profile U/U_∞ , normal Reynolds stresses $u^2(x)/U_\infty^2$, $v^2(x)/U_\infty^2$, and turbulent KE $kt(x)/U_\infty^2$ comparison with BANC wind tunnel data.	18
Figure 3.6 Parametric Grids from top, Baseline, trip 0.065c, trip 0.41c, trip 0.935c. Note: outline of cases 1-3 shown for clarity.	21
Figure 3.7 Baseline vs. tripping, and experimental data for chord-wise distribution of the time-averaged mean surface pressure coefficient, $C_p (x/l_c)$	22
Figure 3.8 U-velocity profile U/U_∞ , normal Reynolds stresses $u^2(x)/U_\infty^2$, $v^2(x)/U_\infty^2$, and turbulent KE $kt(x)/U_\infty^2$ comparison with BANC wind tunnel data.	22
Figure 3.9 Instantaneous 2D dilatation field, cases from the top, Baseline, trip 0.065c, trip 0.41c, and trip 0.935, respectively.	23
Figure 3.10 Instantaneous 2D Baseline case, pressure field with acoustic waves.....	25
Figure 3.11 Acoustic field data extraction locations far-field (left), directivity (right)....	26
Figure 3.12 Far-field one-third octave band TBL-TE noise spectrum (re $2e-5$ Pa) with BANC data for comparison.	28
Figure 3.13 Far field 1/3-octave band TBL-TE noise directivity patterns $\overline{prms(\theta)} / \overline{prms(\theta)}$, from top CFD data, bottom BANC comparison data for Case 1.....	29
Figure 3.14 Pressure time history for pressure probe located at station $(x, y) = (1, 2.5)$ for 2D duration non-dimensional time $\tau = 19-20$	30
Figure 4.1 The 2D and 3D Baseline (left), and trip 0.41c (right), whole grid (top), and close-up of airfoil-mesh region showing block overlap region (bottom), respectively....	33
Figure 4.2 Instantaneous dilatation field at $\tau = 36$ for 2D (left), and 3D (right) plots for the Baseline (top) and trip 0.41c (bottom) cases, respectively.	35
Figure 4.3 Instantaneous dilatation field plots at $\tau = 36$ for 2D (top two) and 3D	

(bottom two) Baseline (first, third) and trip 0.41c (second, fourth) cases, respectively...	36
Figure 4.4 Instantaneous pressure field plots at $\tau = 36$ for 2D (top two) and 3D (bottom two) Baseline (first, third) and trip 0.41c (second, fourth) cases, respectively.	37
Figure 4.5 Instantaneous z-vorticity field plots at $\tau = 36$ for 2D (top two) and 3D (bottom two) Baseline (first, third) and trip 0.41c (second, fourth) cases, respectively...	38
Figure 4.6 Mean pressure coefficient for the 3D Baseline case, trip 0.41c case, and experimental data.	39
Figure 4.7 3D Mean skin friction coefficient comparing the Baseline, and trip cases.	40
Figure 4.8 Prms on the SS of the airfoil for the Baseline, and trip 0.41c cases.....	41
Figure 4.9 Fluctuations in tangential velocity for Baseline, and trip 0.41c cases on the airfoil surface.	42
Figure 4.10 P'rms on the SS and PS of the airfoil for the Baseline, and trip 0.41c cases.	43
Figure 4.11 V'rms on the SS and PS of the airfoil for the Baseline, and trip 0.41c cases.	44
Figure 4.12 Comparison of 2D base (blue) and trip (orange) vs. 3D base (green) and trip (red) cases, respectively, SS boundary-layer profiles. Top) Averaged tangential U-velocity, Bottom) $U_{t,rms}$ -velocity.	45
Figure 4.13 The 3D mean velocity profiles $u^* = u/u_\infty$, $v^* = v/v_\infty$, $w^* = w/w_\infty$, and the mean fluctuating components of velocity $(u'u')^*$, $(v'v')^*$, $(w'w')^*$, and TKE are taken at 1.0038c for both cases.....	46
Figure 4.14 2D and 3D pressure time histories for pressure probe located at station $x/c = 0.42$ for duration non-dimensional time $\tau = 19$ to 19.5 (top), and $\tau = 19$ to 20 (bottom).....	47
Figure 4.15 2D and 3D pressure time histories for pressure probe located at station $x/c = 0.989$ for duration non-dimensional time $\tau = 19$ to 19.5 (top), and $\tau = 19$ to 20 (bottom).....	48
Figure 4.16 Narrow band power spectral density of the airfoil SS surface pressure at $x/c = 0.42$ (top left), $x/c = 0.50$ (top middle), $x/c = 0.60$ (top left), alongside surface one-third octave band data at the same locations; with surface one-third octave band data at $x/c = 0.989$ (lower).....	49
Figure 4.17 One-third octave band power spectral density at $x/c = 0.989$ compared with experimental data (Herr, 2016)	50
Figure 4.18 Suction side (SS) and pressure side (PS) pressure probe locations on the surface of the airfoil at $x/c = 0.42, 0.50, 0.60,$ and 0.989 to compare with BANC data. .	50
Figure 4.19 Instantaneous dilatation field plots at $\tau = 36$ for 2D (top two) and 3D (bottom two) Baseline (first, third) and trip 0.41c (second, fourth) cases, respectively...	52
Figure 4.20 Instantaneous pressure field plots at $\tau = 36$ for 2D (top two) and 3D (bottom two) Baseline (first, third) and trip 0.41c (second, fourth) cases, respectively...	54
Figure 4.21 Instantaneous pressure field at $\tau = 36$ for 2D (left), and 3D (right) plots for	

the Baseline (top) and trip 0.41c (bottom) cases, respectively.	55
Figure 4.22 The data extraction location from $1 < x/c < 3$ within the near wake to quantify vortex shedding.....	56
Figure 4.23 The (p') rms was measured from $1 < x/c < 3$ within the near wake for 1024 time steps to quantify the average pressure fluctuations.	56
Figure 4.24 Instantaneous z-vorticity field plots at $\tau = 36$ for 2D (top two) and 3D (bottom two) Baseline (first, third) and trip 0.41c (second, fourth) cases, respectively...	58
Figure 4.25 The RMS of vorticity was measured from $1 < x/c < 3$ within the near wake for 1024 time steps to quantify the average vorticity fluctuations.....	59
Figure 4.26 3D vorticity data extracted ($1 < x/c < 3$, $-0.04 < y/c < 0.04$) for 1024 time steps, and RMS to see where the peak vorticity fluctuations occur.....	60
Figure 4.27 3D vorticity data extracted ($-0.04 < y/c < 0.04$) for 1024 time steps, and RMS to see where the peak vorticity fluctuations occur.....	60
Figure 4.28 Non-normalized far field TBL-TE noise directivity patterns, $p_{rms}(\theta)$, same scale (top), relative scale (bottom) for 1 kHz band (left), 2 kHz (middle), and 5 kHz (right).	62
Figure 4.29 Normalized 3D far field 1/3-octave band noise directivity patterns as specified by the BANC workshop for 1 kHz band (left), 2 kHz (middle), and 5 kHz (right), with DLR data (Herr, 2015).....	62
Figure 4.30 Far field one-third octave band for the baseline, and trip 0.41c cases at $2.5c$ above and below the TE with comparison data.	63
Figure 4.31 3D pressure time history for pressure probe located at station $(x, y) = (1, 2.5)$ for duration non-dimensional time $\tau = 19$ to 19.7	64
Figure 4.32 Far field data extraction location for further probing.....	65
Figure 4.33 1/3-octave band far field noise with spectra, at $r = 1m$, $\theta = 5$ deg. (top left), $\theta = 120$ deg. (top right), $\theta = 240$ deg. (bottom left), and $\theta = 355$ deg. (bottom right), respectively.....	66

SYMBOLS

c	Chord
C	Coefficient
dt	Discretization of time
e	Flow specific energy
f	Frequency
$\vec{F}, \vec{G}, \vec{H}$	Viscous flux vector in u, v, w-direction, respectively
h	Height
J	Transformation Jacobian
k	Kinetic energy
M	Mach number
p	Pressure
p'	Acoustic pressure
\vec{Q}	Solution vector
r	Radius
Re	Reynolds number
\vec{S}	Source term
t	Time
t	Thickness
T	Temperature
u, v, w	Tangential, normal, and span-wise velocities, respectively
U	Free stream velocity
α	Angle of attack
Δ	Delta, spatial discretization
γ	Specific heat ratio, 1.4
ρ	Density
θ	Angle in degrees
<i>Subscripts:</i>	
$1, 2, 3$	Indicating u, v, w-velocities, respectively
i, j, k	Indicating x, y, z-directions, respectively
D	Drag
f	Skin-friction
L	Lift
M	Moment
P	Pressure
rms	Root mean square
τ	Tau, non-dimensional time
ξ, η, ζ	Generalized curvilinear computational coordinates

ABBREVIATIONS

2D, 3D	Two-, and three-dimensional, respectively
AFB	Air Force Base
AFRL	Air Force Research Laboratory
BANC	Benchmark for Computations in Airframe Noise
BL	Boundary-layer
BPM	NASA code
CAA	Computational aeroacoustics
CFD	Computational fluid dynamics
DES	Detached-eddy simulations
DLR	German Aerospace Center
DNS	Direct Numerical Simulation
EN ISO	International Organization for Standardization in Engineering
FDL3DI	USAF Research code
FFT	Fast Fourier Transform
IAG	Institute of Aerodynamics and Gas Dynamics
ILES	Implicit Large-Eddy Simulations
LBL	Laminar boundary-layer
LE	Leading-edge
LES	Large-Eddy Simulations
NACA	National Advisory Committee for Aeronautics
NASA	National Aeronautical Space Administration
PS	Pressure-side
RANS	Reynolds-averaged Navier-Stokes
RMS	Root mean square
SPL	Sound pressure level
SS	Suction-side
TBL	Turbulent boundary-layer
TE	Trailing-edge
TEB	Trailing-edge bluntness
TEN	Trailing-edge noise
TKE	Turbulent kinetic energy
T-S	Tollmien-Schlichting
UAV	Unmanned Aerial Vehicles
URANS	Unsteady Reynolds-averaged Navier-Stokes
VS	Vortex shedding

ABSTRACT

Lewis, James Benjamin MSAE, Embry-Riddle Aeronautical University, August 2017. Effect of Boundary-Layer Tripping on Turbulence Generation, And Trailing-Edge Noise in Transitional Airfoils.

The need arises for developing quiet aircraft and silent Unmanned Aerial Vehicles (UAVs) to minimize the environmental effects as well as for stealth missions. We focus here on attempting to directly predict the noise associated with airframe by considering a single isolated airfoil. Developing an ability to directly predict the radiated noise and how it is generated is a first step for passive or active control of the generated noise. We choose herein a NACA0012 airfoil and specific flow condition to test whether we can directly predict the sound in accordance with the corresponding experimental data identified in the Benchmark Problems for Airframe Noise Computations (BANC, 2016). We implement a high-fidelity large-eddy simulation code initially developed by the U.S. Air Force Research Laboratory. To understand the mechanisms involved and possibly control it, we considered both the case of clean (untripped) airfoil as well as a tripped one.

Our results for flow near the airfoil surface show that our prediction of the boundary layer and turbulence intensities are consistent with that of experimental results. Tripping, while it does modify the initial transition process, has little effect on the flow fluctuations near the trailing edge.

The calculated spectra of the acoustic field as well as its directivity were found to be in close agreement with the experimental data. Tripping had little effect, if any, on the radiated sound. This indicates that, for this case, the dominant noise source is the scattering of the boundary layer fluctuations at the trailing edge.

1. Introduction

Air vehicle noise is of critical concern to the aerospace industry, and NASA has set a goal of 10 dB reduction of airframe noise in the near-term. In today's market, computational tools have come a very long way to aid in the process of air vehicle design to become the third pillar of preliminary design studies alongside wind-tunnel testing, and flight-test vehicles. Direct Numerical Simulation (DNS), where all scales in the flow field are resolved, and Large Eddy Simulation (LES), where the large scales are directly computed and the small scales are modeled, are computational tools that are increasingly becoming more affordable and gaining the ability to benefit the conceptual design, and preliminary design process. This study aims to employ implicit LES on airfoil geometry to address the goal of airframe noise reduction. Specifically, passive geometry modifications such as boundary-layer trips are investigated to study their effect on acoustics and potential mitigation of noise.

1.1. Background Information

In this study, the NACA0012 airfoil was chosen to enable comparison with experimental data. Implicit LES computational tools were utilized for the present study specifically because the high-fidelity accuracy solver allows users to resolve acoustics when calculating the full Navier-Stokes equations for a fluid flow study. We focus here on the airfoil trailing-edge noise (TEN), which is relevant for rotorcraft, propellers, UAVs, wind turbines, and in fixed-wing subsonic landing. The objective of this work is to pursue research aimed at understanding the physics behind aerodynamic noise generation.

1.2. Motivation

Having served in the military there is a deeper connection that exists as an engineer designing air vehicles for combat deployment. Mitigating airframe noise would not only bring a new level of stealth to U. S. Air Force missions, but could effectively save lives bringing a higher purpose to the work.

Nature has been solving complex problems for millennia. In the realm of acoustics and flight, no creature is more equipped, with over a million years of evolution toward noise suppression, and whose geometry is more relevant to the present study than that of the owl. Upon descent toward prey owls use a leading-edge comb, trailing-edge feathers that form a fringe, and a fluffy-soft down over the Suction Side (SS) of the wing as stealth to suppress the aeroacoustics noise that would otherwise be generated by their body's quick descent through the air (Lilley, 1998). These three geometry modifications, what Lilley calls "owl technology", illuminate the relationship between airfoil geometry, and corresponding noise generating sources, namely the LE geometry, TE geometry, and airfoil boundary-layer surface. This study would attempt to harness this knowledge and focus primarily on TE noise, as it has been shown to be the most dominant source of airfoil self-noise (Brooks et al., 1989). A passive flow control device, such as a boundary-layer trip, was sought as a solution for the sake of simplicity and practicality.

1.3. Sources of Noise

Critical to understanding the results of this study is the knowledge of the flow about the airfoil, and the associated noise generation mechanisms. In the absence of freestream turbulence, the isolated airfoil essentially experiences five airfoil self-noise mechanisms depending on flow conditions: turbulent boundary-layer trailing-edge (TBL-TE) noise,

laminar-boundary-layer vortex-shedding (LBL-VS) noise, separation-stall noise, trailing-edge-bluntness vortex-shedding (TEB-VS) noise, and tip vortex formation noise. Of these, TBL-TE noise, and LBL-VS noise are two of the most important self-noise mechanisms. At high Reynolds numbers TBLs develop over most of the airfoil. Noise is produced within the suction side (SS) and pressure side (PS) TBLs, at the TE, and into the near wake leading to TBL-TE noise. At low Reynolds numbers, largely LBLs develop over one or both sides of the airfoil, whose instabilities begin somewhere in the BL near the LE, and grow exponentially downstream. This results in VS with associated broadband, and tonal noise from the TE (Golubev et al., 2011).

Only three of these noise sources are relevant in this study: turbulent boundary-layer TE noise, laminar boundary-layer vortex-shedding noise, and trailing-edge bluntness vortex-shedding noise. Because the study is at zero incidence, separation stall noise does not apply as separation is largely a function of angle of attack (Abbott, 1949). Furthermore, the study is span-wise periodic, which eliminates any possible tip-vortex formulation noise. In the literature, no data exists at the Reynolds number studied herein where a separation bubble is shown to exist, and no feedback loop with associated tones. However, if a great portion of the BL is laminar, some LBL VS noise may exist. Therefore, it was left to be investigated by the current study which will show that at this Reynolds number some portion of the BL is laminar.

The TE geometry of the airfoil studied here is purposefully rounded to create an O-grid and eliminate a singularity at the TE as was done in (Nguyen, 2016). The TE radius, $r = 0.004c$, and the maximum height of the rounded TE is the diameter of the rounded TE, or 0.8% chord. This geometry leaves few primary noise generation mechanisms, TBL-

TE noise, and LBL-VS noise, as well as TEB-VS noise as possible candidates to be considered. These mechanisms are shown in Figure 1.1 (Brooks et al., 1989):

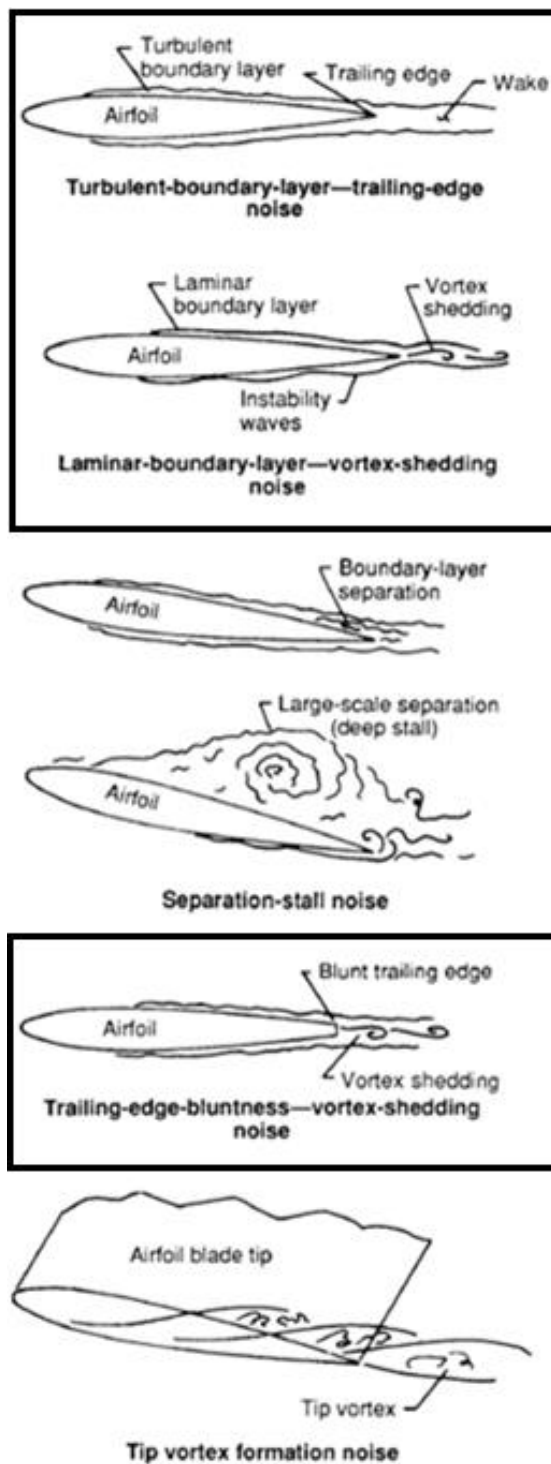


Figure 1.1 Airfoil self-noise mechanisms, with relevant mechanisms outlined (Brooks et al., 1989).

1.4. Previous Work

The Workshop on Benchmark Problems for Airframe Noise Computations (BANC, Herr et al., 2015) has provided a compass and direction for this study. The objective of the workshop is to assess the present computational capabilities in physics-based prediction of broadband TBL-TE noise, with the goal of advancing the state-of-the-art with a combined effort. Participants covered the full bandwidth of existing semi-empirical, theoretical, hybrid, acoustic analogy or CAA, in combination with unsteady Reynolds-Averaged Navier-Stokes, LES, and detached eddy simulation. Most importantly, the workshop focus is the same as that of the present study which is TBL-TE noise, and compares data of a NACA0012 with and without tripping at a Reynolds number of 1.5 million.

Parametric experiments attempting to reduce TEN by addressing the TBL and varying the porosity of the airfoil blade surface with flow-permeable edge modifications were conducted by Herr et al. (2015). Symmetrical tripping on the SS & PS sides was employed in this study on a NACA0012 airfoil at 9.25% chord, and 40% chord, establishing well-defined TBL transition locations to address classical TEN related to BL turbulence characteristics.

A related wind tunnel test was performed at the Institute of Aerodynamics and Gas Dynamics (IAG) (Herrig et al., 2008). In this experiment, the NACA0012 airfoil of 0.4m chord was tested at $U=60$ m/s, corresponding to $M=0.175$, Reynolds number of 1.6 million, at zero angle-of-attack, which is very close in comparison to the present study's set-up. It was discovered during the test to best avoid blunt TE noise the TE needed to be sharpened to a very fine 0.22 mm, corresponding to TE thickness of $h = t/c = 0.00055$. While their

study focused primarily on the effect of TE bluntness to far field noise, a small subset of data using BL tripping was created showing a reduction of the overall spectral maximum.

With respect to numerical work, a high-fidelity LES study by Winkler et al., (2009) was performed in which a BL trip was employed, and the effects of which were well documented. At relatively low Reynolds number (on the order $\approx 10e5$), large portions of the BL were shown to be laminar leading to the development of T-S instability waves with well-known aeroacoustics feedback loop, and broadband humps with regular humps superimposed. It was also observed that artificially tripping the BL removes this extra instability noise mechanism. In another high-fidelity numerical study, it was acknowledged that tripping a transitional BL forces transition to turbulence, thus eliminating the onset of coherent instabilities (Golubev et al., 2013). In another relevant LES study (Garrec & Glorefelt, 2008) with a NACA0012 airfoil, it was suggested that span-wise symmetrical tripping forced transition ensures reproducibility. The study also demonstrated that the most dominant noise source originated from the TBL passing the TE, and showed symmetric BL tripping resulted in no tone noise. Using the ILES code FDL3DI (Golubev et al., 2011), it was reported that tripping ensures a TBL, which is partly responsible for low frequency spectra, while tonal noise is associated with the laminar instabilities. These studies clarify that at moderate Reynolds numbers BL tripping eliminates the laminar boundary-layer vortex-shedding noise.

To expound on this fact, Brooks et al., (1989) used the NACA0012 airfoil, with and without a geometrical BL trip, and their predictions determined that TBL-TE noise and separation noise could be scaled from the tripped BL cases, and the LBL-VS noise could be scaled from the untripped cases. They also associated the LBL instabilities

coupled with the acoustic feedback to produce multiple and erratic quasi-tonal noise with the untripped case. They determined that the controlling mechanism of LBL-VS noise is the presence of aeroacoustics feedback loops between the TE and an upstream location where laminar instability occurs. It is worth noting that Brooks et al.'s predictions compared successfully up to Mach number and Reynolds number of 0.5, and 4.6×10^6 , encompassing the present study Reynolds numbers of 1.5 million.

In regard to tonal noise, experiments conducted in Brooks and Hodgson, 1981, discrete tones were emitted by a low α airfoil in laminar flow which was eliminated by inducing turbulent flow by way of artificial tripping of the BL. It was noted that varying experiments with different tripping devices showed that low-frequency tone effects could be attenuated or even eliminated through tripping (Dobrzynski, 2010). In further support of this effect, further experiments by Lawson (1994) showed that the acoustic feedback loop could be broken by the insertion of a BL trip on the PS.

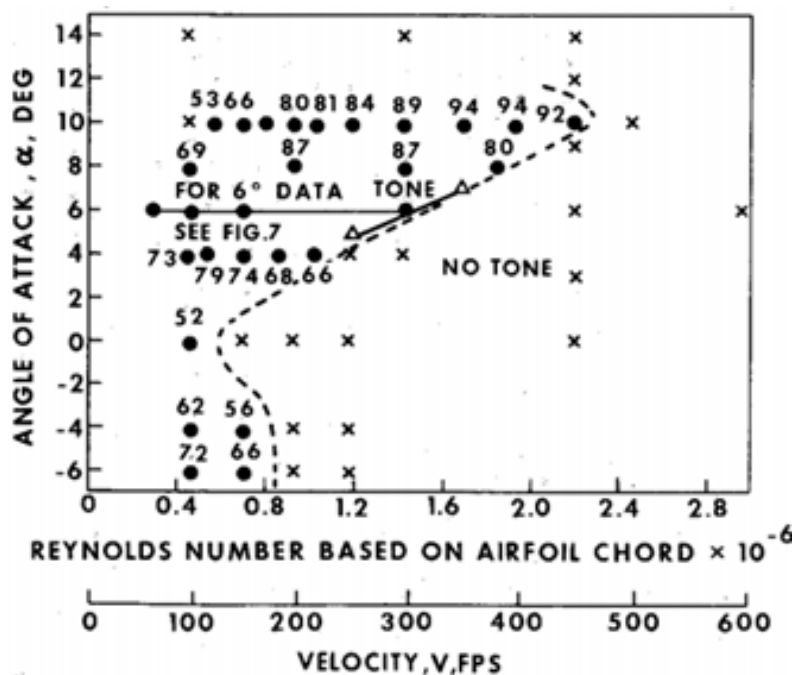


Figure 1.2 Tonal noise regimes of a NACA0012 associated with VS (Paterson, 1973).

Paterson (1973) noted that a BL trip placed forward of 80% chord on the PS would cause the tone to disappear, indicating the tone was associated with the LBL on the PS. His tonal map based on a finite NACA0012 full-span airfoil, shown in Figure 1.2, is quite illuminating. It is interesting to note that about the NACA0012 finite airfoil at zero angle of incidence, there is a certain velocity after which there should be no tonal noise associated with the TE noise. This would indicate that tonal noise is dependent on Reynolds number, and angle of attack, as was shown (Lowson et al., 1994) and Nguyen (2016). For the Reynolds number considered in this study at zero angle of attack, there are no tones generated.

In Casper & Farasat (2004) study of broadband noise associated with TE noise, a BL trip was applied at 15% chord from the LE to ensure a span-wise uniform transition and a fully developed TBL at the TE. In Oerlemans et al. (2007)'s study wind turbine research, it was discerned that in some instances tripping can lead to greater narrow band airfoil self-noise because of the over-thickening of the TBL. In the Sagrado et al. (2006) experiment into discerning trailing-edge noise sources, a trip wire was used at 12.7% chord to ensure the development of a span wise uniform TBL convecting past the TE, and distinguish the fact that TE noise is the main mechanism of broadband noise.

In the following section, we present the numerical methodology. This will be followed by a two-dimensional simulation to assess the abilities of the code. The physical, three-dimensional results are presented in section 4, followed by Conclusions.

2. Computational Methodologies

In developing the CAA field, Large Eddy Simulations are needed to resolve the sound sources (Mankbadi, 1994, Mankbadi et al. 1995). One can use a low-order code with unstructured grid, or a high-order structured grid code (e.g. Mankbadi et al., 2016). In this study, we use the FDL3DI code, which is a high-order structured grid code developed by the U.S. Air Force Research Laboratory (Gaitonde & Visbal, 1999, Visbal & Gaitonde, 1998, 2002). FDL3DI is one of the primary research tools of the CFD group at Wright-Patterson AFB. The code has been successfully used by ERAU's CAA group in the past to study aeroacoustics (Golubev et al., 2012, Mankbadi et al., 2015). This section presents the formulation and scheme of the code employed.

The numerical code solves the compressible Navier-Stokes equations represented in strong conservative, time-dependent form in the generalized curvilinear computational coordinates (ξ, η, ζ, τ) transformed from the physical coordinates (x, y, z, t) :

$$\frac{\partial}{\partial \tau} \left(\frac{\vec{Q}}{J} \right) + \frac{\partial \vec{F}_i}{\partial \xi} + \frac{\partial \vec{G}_i}{\partial \eta} + \frac{\partial \vec{H}_i}{\partial \zeta} + \frac{1}{Re} \left[\frac{\partial \vec{F}_v}{\partial \xi} + \frac{\partial \vec{G}_v}{\partial \eta} + \frac{\partial \vec{H}_v}{\partial \zeta} \right] = \vec{S} \quad (2.1)$$

The solution vector $\vec{Q} = (\rho, \rho u, \rho v, \rho w, \rho e)$ is defined in terms of the flow density ρ , Cartesian flow velocity components (u, v, w) , and flow specific energy,

$$e = \frac{T}{\gamma(\gamma-1)M_\infty^2} + \frac{1}{2}(u^2 + v^2 + w^2) \quad (2.2)$$

The assumption of perfect gas relationship $p = \rho T / \gamma M_\infty^2$ connects the flow pressure p , temperature T , and the freestream Mach number M_∞ (γ is the specific heat ratio). The other variables in Eq. (2.1) include the inviscid flux vectors defined by,

$$\vec{F}_i = \begin{bmatrix} \rho \hat{u} \\ \rho u \hat{u} + \hat{\xi}_x p \\ \rho v \hat{u} + \hat{\xi}_y p \\ \rho w \hat{u} + \hat{\xi}_z p \\ (\rho e + p) \hat{u} - \hat{\xi}_t p \end{bmatrix}, \vec{G}_i = \begin{bmatrix} \rho \hat{v} \\ \rho u \hat{v} + \hat{\eta}_x p \\ \rho v \hat{v} + \hat{\eta}_y p \\ \rho w \hat{v} + \hat{\eta}_z p \\ (\rho e + p) \hat{v} - \hat{\eta}_t p \end{bmatrix}, \vec{H}_i = \begin{bmatrix} \rho \hat{w} \\ \rho u \hat{w} + \hat{\zeta}_x p \\ \rho v \hat{w} + \hat{\zeta}_y p \\ \rho w \hat{w} + \hat{\zeta}_z p \\ (\rho e + p) \hat{w} - \hat{\zeta}_t p \end{bmatrix}, \quad (2.3)$$

The transformation Jacobian, $J = \partial(\xi, \eta, \zeta, \tau) / \partial(x, y, z, t)$, the metric quantities defined, e.g., as $\hat{\xi}_x = (J^{-1}) \partial \xi / \partial x$, etc., and the transformed flow velocity components,

$$\begin{aligned} \hat{u} &= \hat{\xi}_t + \hat{\xi}_x u + \hat{\xi}_y v + \hat{\xi}_z w \\ \hat{v} &= \hat{\eta}_t + \hat{\eta}_x u + \hat{\eta}_y v + \hat{\eta}_z w \\ \hat{w} &= \hat{\zeta}_t + \hat{\zeta}_x u + \hat{\zeta}_y v + \hat{\zeta}_z w \end{aligned} \quad (2.4)$$

The viscous flux vectors, \vec{F}_i , \vec{G}_i , and \vec{H}_i , are defined, while \vec{S} represents the source term which allows incompressible unsteady vortical perturbation to be introduced into the flow field. All flow variables are normalized by their respective reference freestream values except for pressure, which is normalized by dynamic pressure, $\rho_\infty u_\infty^2$.

The governing equations are represented in the original unfiltered form and are unchanged in laminar, transitional or fully turbulent regions of the flow. To provide further details on the code's employed ILES procedure in which a high-order low-pass filter operator is applied for additional dissipation during the solution process.

The code employs a finite-difference approach to discretize the governing equations, with all the spatial derivatives obtained using the high-order compact-differencing schemes (Lele, 1992). For the quasi-wing section computations of the current work, a 6th-order scheme is used. At boundary points, higher-order one-sided formulas are utilized which retain the tridiagonal form of the scheme and the time marching is accomplished by incorporating a 2nd-order iterative, implicit approximately-factored procedure as described.

3. Two-Dimensional Results

Two-dimensional preliminary analysis was conducted to be able to do some quick runs before moving to the computationally-intensive 3D simulations.

3.1 Grid and Boundary Conditions

In previous numerical 2D studies by ERAU's CAA group, a 1281 x 789 O-mesh was used on the NACA0012 airfoil and efficiently partitioned into sets of overlapped blocks assigned to different processors during parallel implementations (Golubev et al., 2013). This grid was the foundation of the current study, but expanded by double the points in the y-direction to maintain suitable resolution at high Reynolds number as necessitated by the current study. The 2D mesh was refined to satisfy Δy^+ conditions at a higher Reynolds number for the present study. As illustrated in Figure 3.1, the mesh is carefully clustered near the airfoil surface to achieve adequate spatial resolution. For the baseline characteristic flow condition with Mach number, $M = 0.1664$ and Reynolds number, $Re_c = 1.5 \times 10^6$, such grid refinement corresponds to the non-dimensional values of $\Delta y^+ \approx 0.77$ and $\Delta x^+ \approx 150$, with 24 grid points clustered in the region $0 < y^+ < 10$. With respect to the wall-normalized normal spatial resolution, $(\Delta n_+)_{max} = 0.797$, and the 3D grid wall-normalized span-wise spacing, $(\Delta z_+)_{max} = 63.9$, as the 2D grid must have at least 3-points in z for computations. Figure 3.1 illustrates the 2D baseline grid:

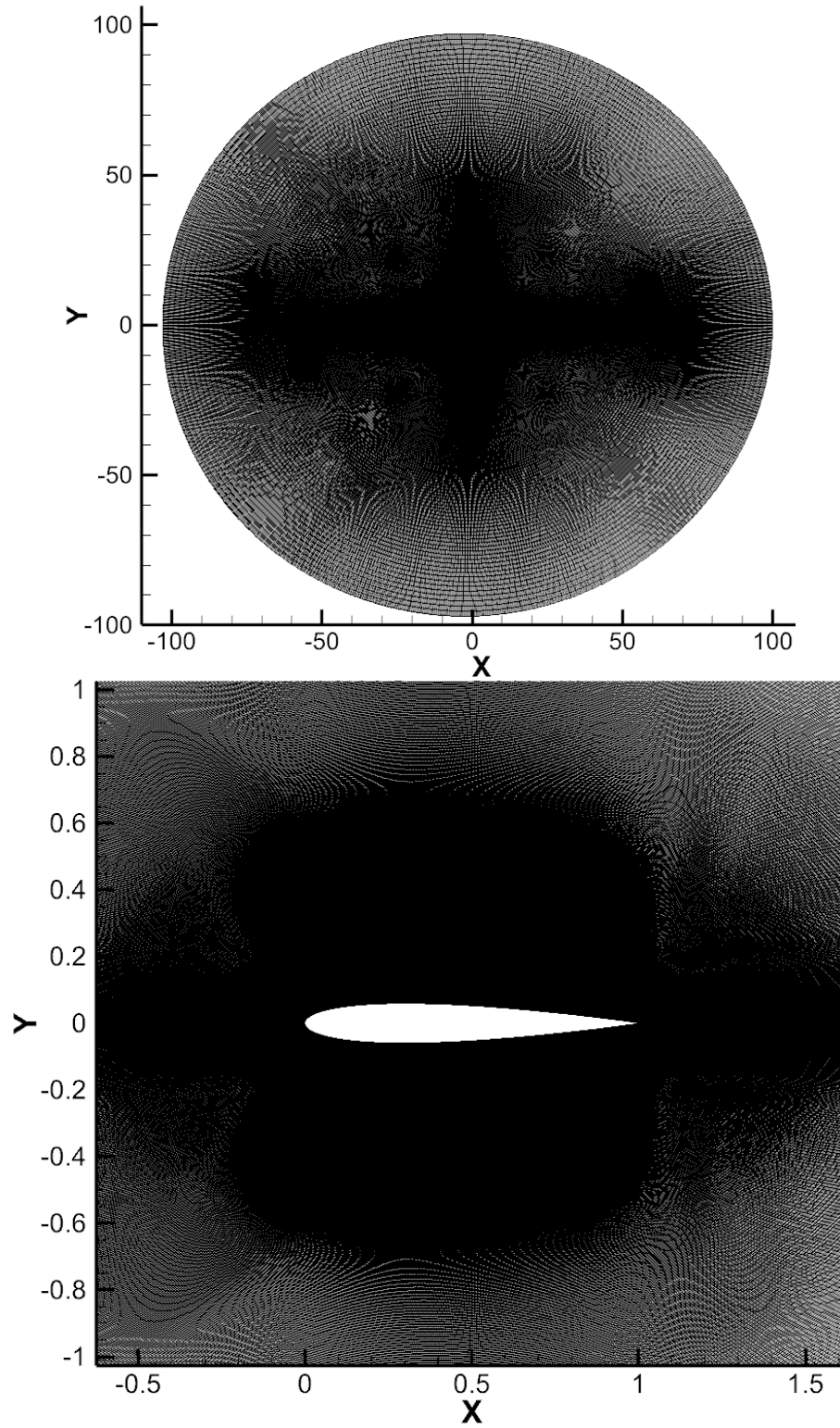


Figure 3.1 Baseline 2D grid far field to $r=100$ chord (top), to near field displaying extensive mesh refinement (bottom).

To conform to the subsonic flight regime of interest, and to align with the BANC Workshop matrix, the Mach number of 0.1664 was used for flow simulations. As mentioned, this subsonic flight regime is closest to that of UAVs and wind turbines. To simulate full-scale study, and to assure turbulence noise generation, the Reynolds number of 1.5 million was implemented. To focus the study as a baseline, and hone in on what is believed to be the primary mechanism of pure trailing-edge noise, the zero angle of attack configuration was selected. This flight condition corresponds closely to the Case 1 simulation matrix study within the BANC Workshop (Herr et al., 2015). Table 3.1, specifies the simulated flow condition:

Table 3.1: Case 1 simulation matrix for the BANC Workshop (Herr et al., 2015).

Airfoil	l_c, m	$U_\infty, m/s$	M_∞	Re	T_∞, K	$\rho_\infty, kg/m^3$	P_∞, Pa	$\alpha, ^\circ$
NACA0012	0.4	56.0	0.1664	1.50E+06	281.5	1.181	95,429	0

Each case of the simulation was setup the same with respect to achieving high quality aeroacoustics predictions, and being of comparable quality to validated studies. The baseline numerical set-up employs a physical time step of 0.675e-6 seconds, or 1.41e-6, corresponding to code non-dimensional time step of 9e-5, or 4.5e-5, for the baseline or tripped case, respectively. It is believed the tripped case needed a finer time step to resolve the fine BL dynamics in the solution in the region just after the trip. For each case simulation, the flow conditions were run to steady-state after marching for 225,000, or 450,000, steps to $\tau = 20.25$ cycles. Twenty cycles was a conservative length of time chosen by monitoring the transient in the solution. It was determined that after 20 cycles the solution was steady state. After which, the pressure signals were then recorded for over 720,000, or 1,440,000 steps, hence for the baseline set-up collecting the data sample for

0.4634 seconds with the sampling rate of 77.7 kHz achieving the frequency resolution of $\Delta f = 2.158$ Hz. This is comparable to the BANC workshop aggregate sampling rate of 80.6 kHz.

Depending on the case, the baseline and tripped grids were made up of 1 to 4 blocks each with 5 to 11-point overlapping to facilitate accurate interpolation required by the flow solver FDL3DI. NASA's Pegasus v. 5.2 was used as a pre-processor for the over-set meshing, and the AFRL's BELLERO v. 2013 was used in pre-processing for accurate grid decomposition to prepare for large-scale parallel processing (Suhs et al., 2002, Sherer, 2003). Figure 3.2 displays convergence of the aerodynamic forces versus tau:

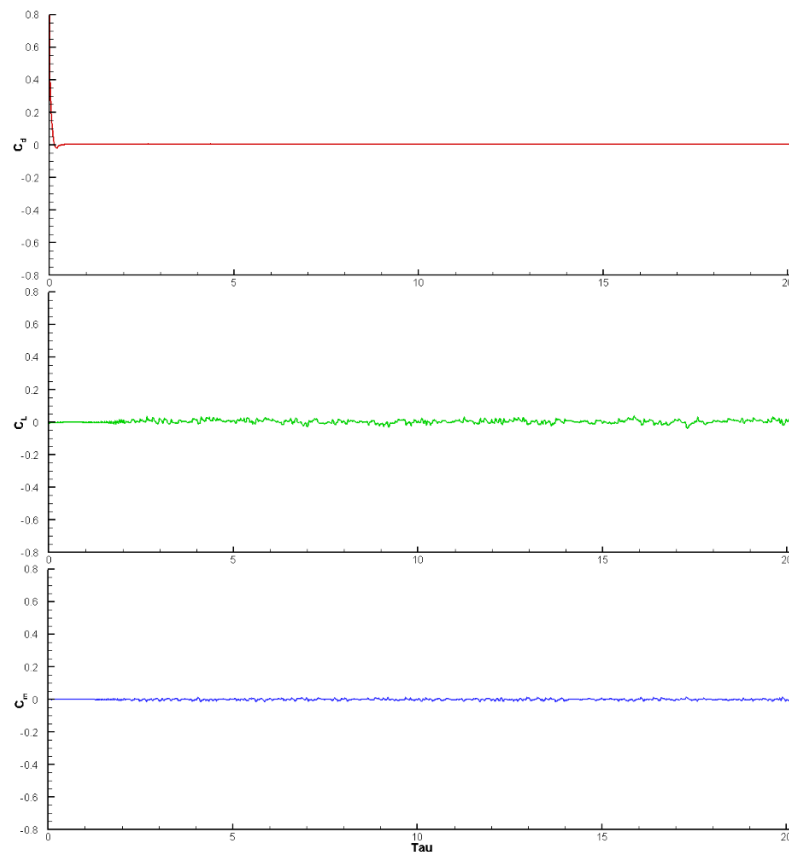


Figure 3.2 Coefficient of Drag (top), Coefficient of Lift (middle), and Moment Coefficient (bottom) vs. non-dimensional time for the baseline case of an untripped NACA0012 airfoil.

3.2 Preliminary Verifications

As previously mentioned, a portion of this work stems from a study of the Workshop on Benchmark Problems for Airframe Noise Computations (BANC), whose objective is to assess the present day computational capability of physics-based flow field solvers in the realm of airframe noise problems, specifically broadband trailing-edge noise predictions. The flow-solvers involved in the BANC Workshop cover the full bandwidth of existing semi-empirical, theoretical, and hybrid methods, approaches based on acoustic analogy or CAA (computational aeroacoustics) in combination with unsteady Reynolds-averaged Navier-Stokes (URANS), large-eddy simulation (LES), detached-eddy simulation (DES) or RANS with stochastic turbulence models.

NASA's BPM (NAFNOISE) code (Brooks et al., 1989), named for Brooks, Pope, and Marcolini, was created when performing airfoil self-noise wind-tunnel testing and was incorporated into the BANC Workshop. The present study compares predicted far field noise spectra with that predicted by BPM. The wind-tunnel tests performed by NASA scientists that laid the foundation for BPM prediction employed NACA0012 airfoils, with and without BL tripping to specifically delineate TBL-TE noise from LBL-VS noise, at varying angles of attack, and Mach 0.1 to 0.5, also varying TE thickness. The case with 0.3048m chord airfoil, sharp TE, at zero angle of attack, at $U=55.5$ m/s, was closest to the present study set up, showed for the tripping case a spectral hump about the 1 kHz band, and a spectral hump about 2 kHz for the untripped naturally transitioning airfoil. It did not however show any noise attenuation, perhaps because trip was achieved by a random application of grit tape strips applied from the LE to about 20% chord. Later studies would employ a more consistent and reproducible geometric BL tripping device.

For comparison and verification of the 2D predictions, a test case with a trip at 6.5% chord was performed for NACA0012 airfoil with the chord, $c = 0.4m$, at the geometric angle of attack, $\alpha = 0^\circ$, and the selected mean flow velocity of 56 m/s ($M = 0.1664$). The numerical analysis follows the simulation matrix for $Re_c = 1,500,000$. This condition was chosen for best direct comparison of the experimental conditions within the BANC Workshop, and to best compare with the numerical data collected for the same purpose.

To analyze the pressure forces on the airfoil, surface data was extracted to analyze the chord-wise distribution of the time-averaged mean surface pressure coefficient along the SS and PS, and to compare it with the experimental data. Calculating the pressure coefficient is useful because the lift coefficient and drag coefficient are simply integrals of $C_{p, u}$ along the surface (Drela, 2014). This lets us keep track of how tripping effects the aerodynamics. The static pressure coefficient normalized by the dynamic pressure, $C_p = (p - p_\infty)/(0.5\rho_\infty u_\infty^2)$, with the axis flipped per convention, shows an adverse pressure gradient after twenty percent chord, with the negative pressure spikes corresponding to the tripped locations. This data does a reasonable job of verifying the accuracy of the CFD results at the surface; Figure 3.3 :

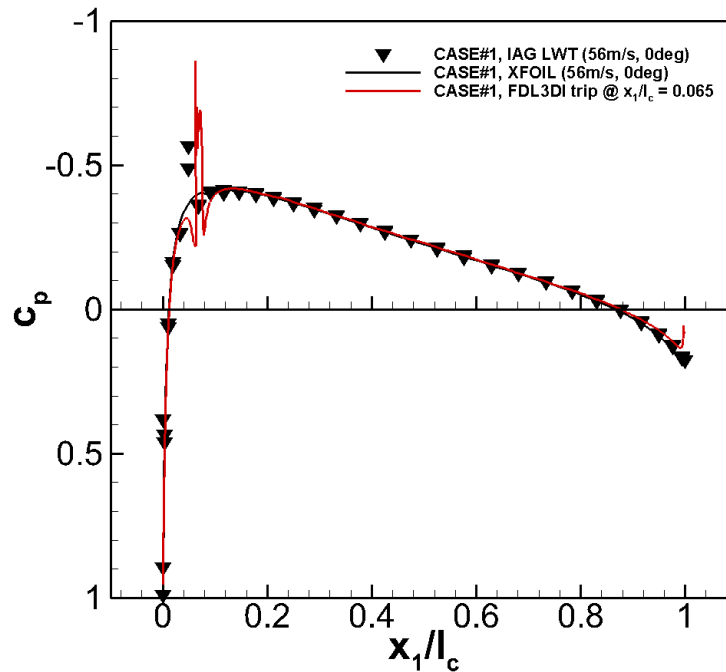


Figure 3.3 Chord-wise distribution of the time-averaged mean surface pressure coefficient, $C_p(x_1/l_c)$.

For comparison, trailing edge flow characteristics at both the SS and the PS in the wake were sought. Data of the chord-normal distributions of the Reynolds stresses non-dimensionalized with the free-stream velocity squared, and the resulting turbulent kinetic energy at 1.0038 chord were extracted. To do so, a rectangular slice of data where $(i, j, k) = (1, 1000, 1)$, at $(x, y) = (1.0038, -0.25 < y < 0.25)$ was analyzed with Figure 3.4 illustrating the region of interest. When post-processing the data after extraction, the data must be passed into MATLAB and the arrays must be multiplied by a scalar for comparison, Figure 3.5:

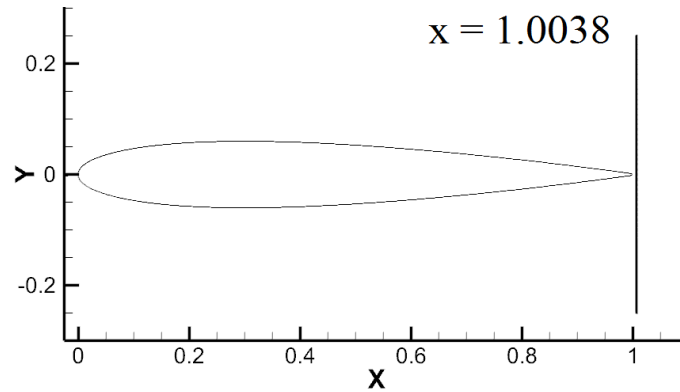


Figure 3.4 Location of flow field data acquisition.

All flow variables within the code FDL3DI have been normalized by freestream values.

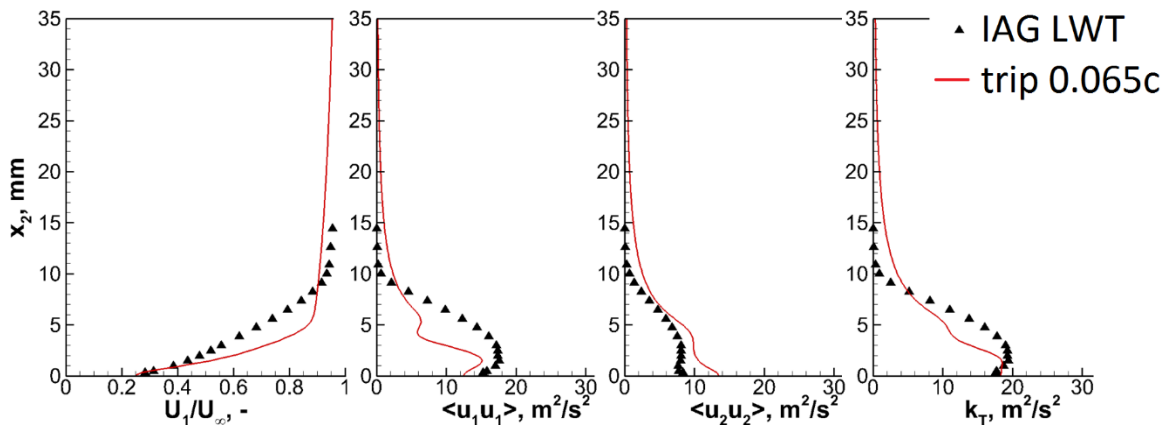


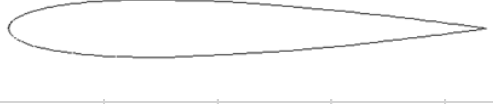
Figure 3.5 U-velocity profile U/U_{∞} , Reynolds stresses $\langle u_1^2(x_2) \rangle / U_{\infty}^2$, $\langle u_2^2(x_2) \rangle / U_{\infty}^2$, and turbulent KE $k_t(x_2) / U_{\infty}^2$ comparison with BANC wind tunnel data.

The Reynolds stresses are an indicator of the turbulence within the BL, with the corresponding turbulent kinetic energy (TKE) term is indicative of turbulence in all flow directions. The u-velocity profile can indicate if a BL is turbulent (thicker) or laminar (thinner). The CFD data trend is comparable to the experimental wind-tunnel data (University of Stuttgart) of the BANC Workshop.

3.3 Effect of Location on Tripping

A parametric study was performed to determine the effect of chord-wise placement of a passive flow control device, a geometrical BL trip, on the flow field, and acoustics. For the current study of noise generation, the baseline grid (no trip) was modified in Pointwise with a rectilinear trip, cross-section 1.5 mm in x, by 0.36 mm in y, symmetric about the pressure-side (PS) and the suction-side (SS) of the airfoil, and uniform in the span-wise direction to preserve infinite 2D. Chronologically, the baseline case (no tripping), named Case 0, followed the leading-edge trip at 0.065c named Case 1, after which a trailing-edge study named Case 2 with the trip at 0.935c was performed. The baseline case is a foundation for the study with which to compare the effect of tripping and determine the chord-wise location of natural transition. The LE trip was used to verify CFD data with the BANC workshop data, and the TE trip case was used to determine whether tripping within an already TBL would further affect acoustics. After studying the initial results, an additional case was run with a trip at 0.41c, Case 3. The 0.41c location was carefully chosen based upon data from the baseline case where it appeared the BL was initiating transition. It was initially thought that triggering artificial transition at the exact point of initial natural transition may be an effective way to influence TE noise. Table 3.2 illustrates the parametric case study:

Table 3.2 Parametric grid study varying trip location.

Trip Location	Cases	Block	Dimension	y^+	Physical Representation
None	0	1	1281x1577x3	0.77	
0.065c	1	1	27x1508x3	0.77	
		2	27x1508x3	0.77	
		3	217x1577x3	0.77	
		4	1053x1577x3	0.77	
0.935c	2	1	25x1507x3	0.77	
		2	25x1507x3	0.77	
		3	219x1577x3	0.77	
		4	1055x1577x3	0.77	
0.41c	3	1	25x1508x3	0.77	
		2	25x1508x3	0.77	
		3	637x1577x3	0.77	
		4	637x1577x3	0.77	

It is important to emphasize careful attention to detail was used to determine the grid spacing to maintain the $y^+ < 1$ recommended by LES recommendations and practices (Georgiadis et al., 2010). The following figure communicates the corresponding grids of the parametric case study, with the Baseline case, tripped grid at 0.065c, tripped grid at 0.41c, and tripped grid at 0.935c cases, from top to bottom, respectively. Note, that besides the baseline case, the tripped case grids show only the outline for clarity. For all cases, the non-dimensional streamwise and surface-normal grid spacing was the same, $\Delta x/c = 2.5 \times 10^{-3}$, and $\Delta y/c = 1.25 \times 10^{-5}$, respectively. Figure 3.6 illustrates the parametric mesh study:

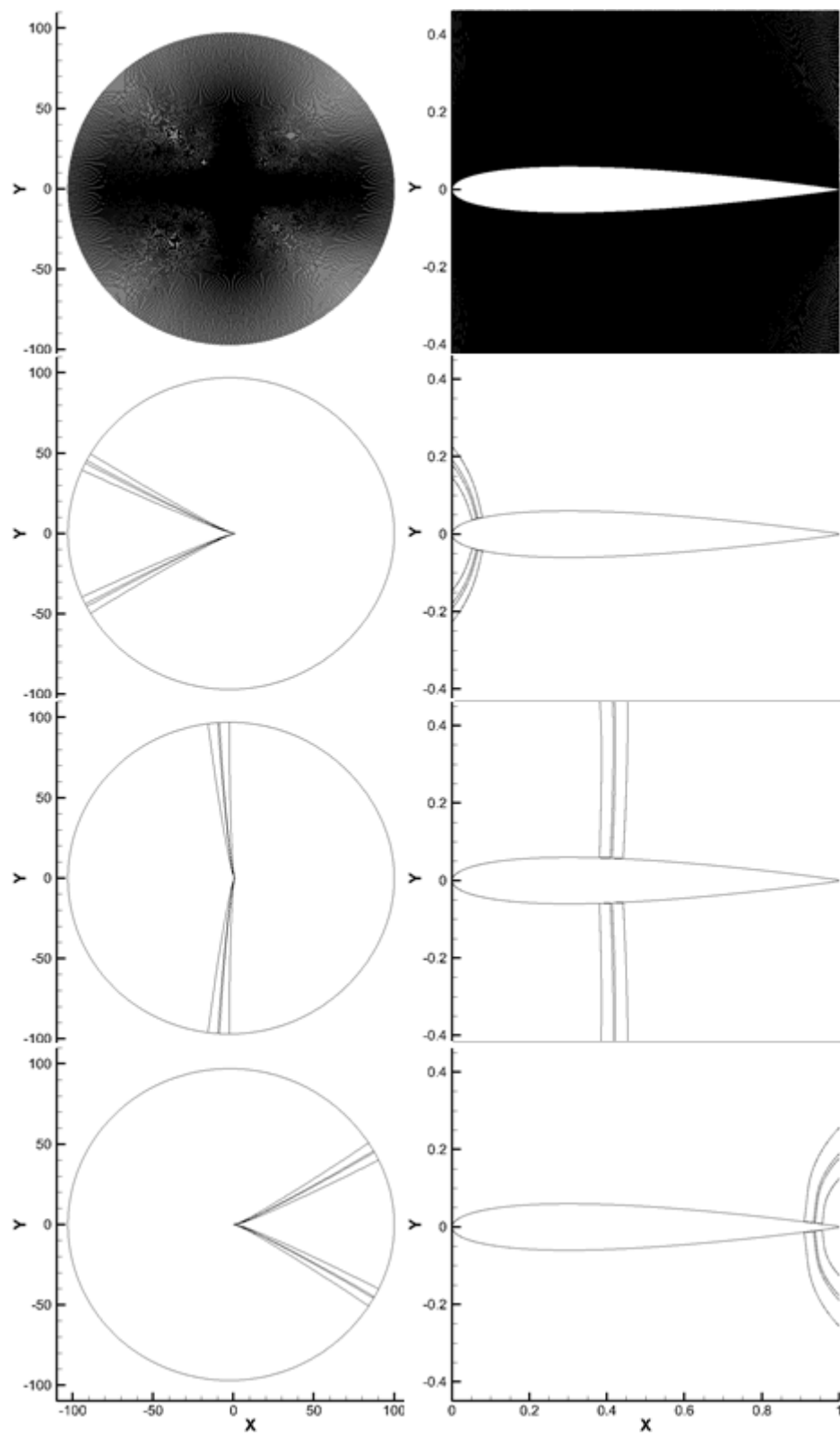


Figure 3.6 Parametric Grids from top, Baseline, trip 0.065c, trip 0.41c, trip 0.935c. Note: outline of cases 1-3 shown for clarity.

To analyze the flow field, surface data was gathered and C_p was calculated, Figure 3.6:

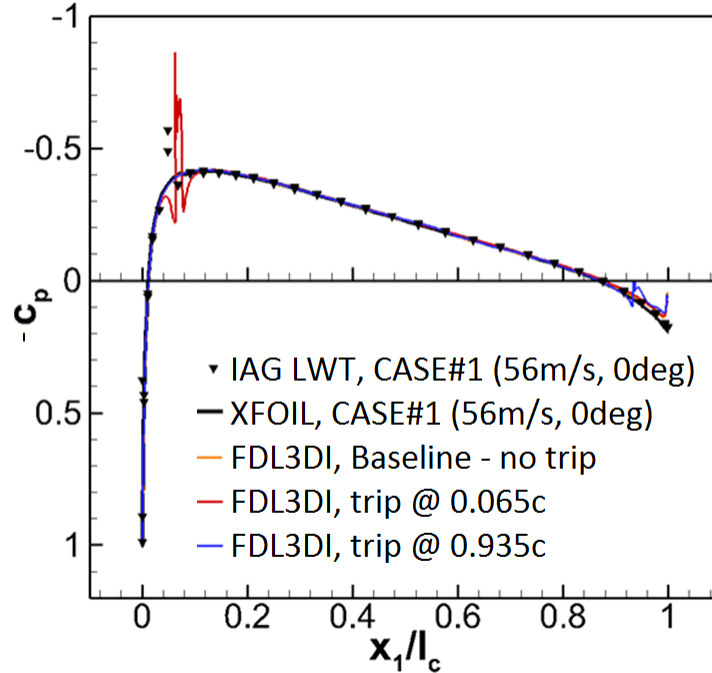


Figure 3.7 Baseline vs. tripping, and experimental data for chord-wise distribution of the time-averaged mean surface pressure coefficient, C_p (x_1/l_c).

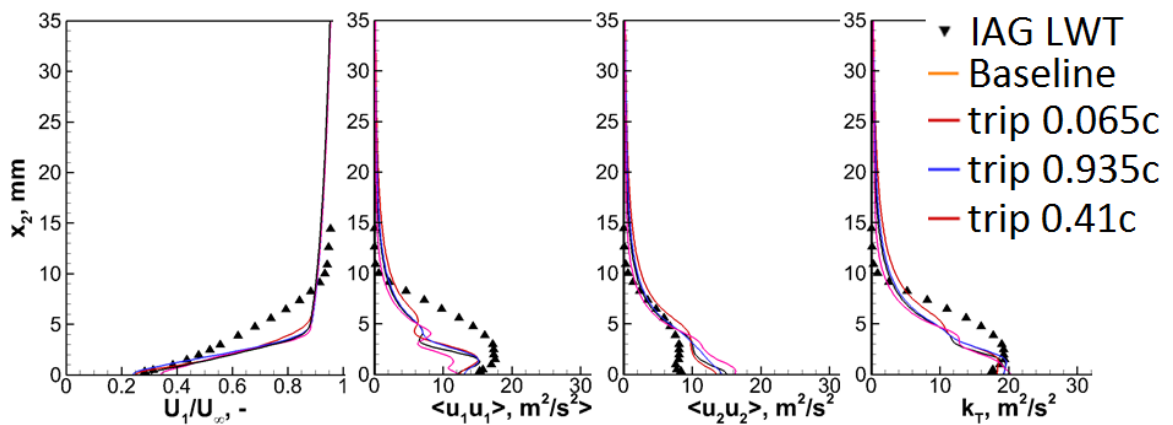


Figure 3.8 U-velocity profile U/U_∞^2 , normal Reynolds stresses $\langle u_1^2(x_2) \rangle / U_\infty^2$, $\langle u_2^2(x_2) \rangle / U_\infty^2$, and turbulent KE $k_t(x_2) / U_\infty^2$ comparison with BANC wind tunnel data.

The results in Figures 3.7 & 3.8 are in reasonable agreement with experiment, but we should be mindful that these computations are only 2D and do not mimic the physics. The

dilatation field was compared, Figure 3.9:

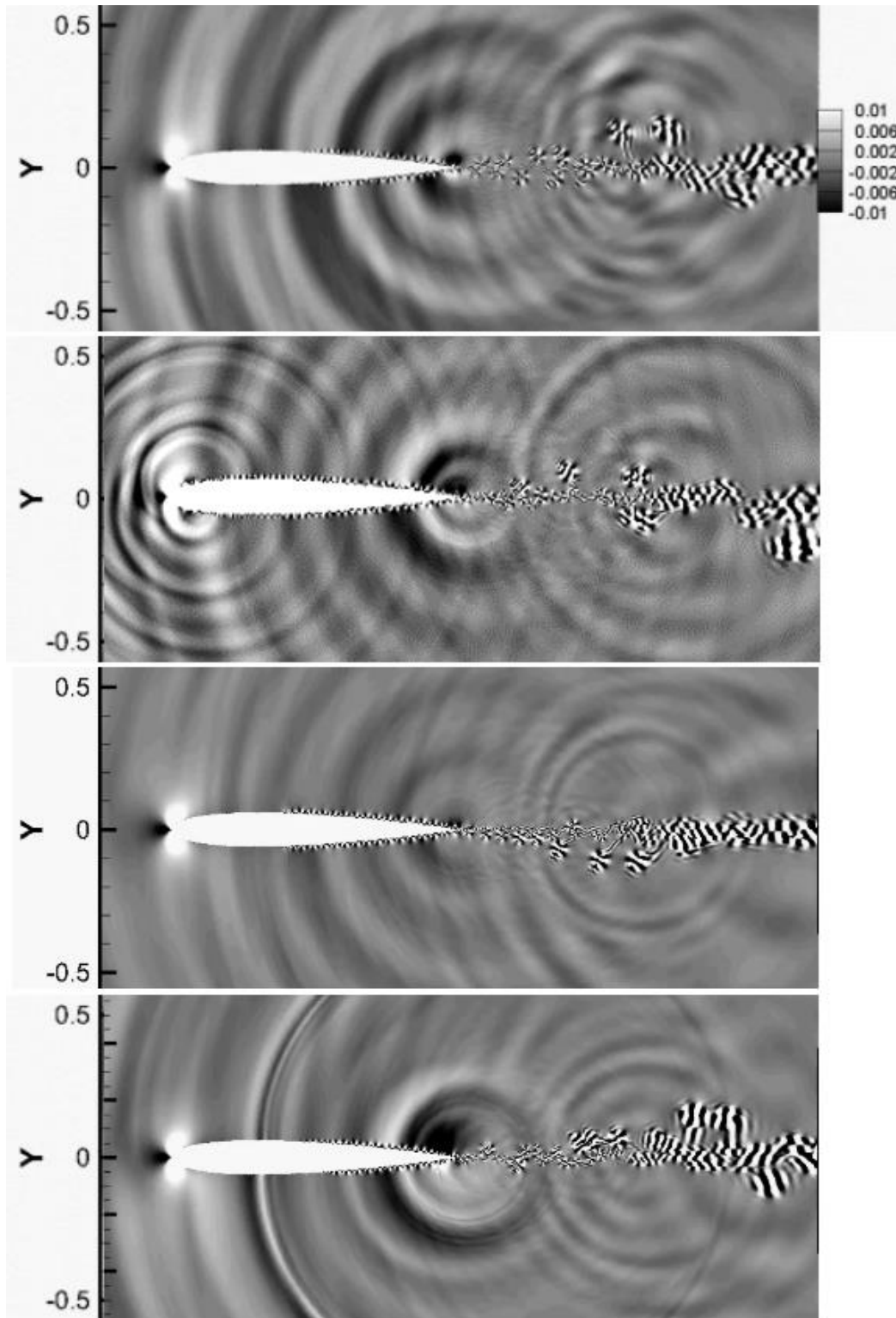


Figure 3.9 Instantaneous 2D dilatation field, cases from the top, Baseline, trip 0.065c, trip 0.41c, and trip 0.935, respectively.

The divergence of velocity parameter, Figure 3.9, is also particularly good at delineating the acoustic wave information within the flow field to communicate sources and sound strength. From these figures, one can observe the presence of the trip, and its location clearly affecting the flow field and acoustic sources about the airfoil. Clearly it appears that the trip in the 0.065c case is creating another source on the PS and SS toward the LE. The trip in the 0.935c case is tripping an already TBL which appears to amplify TE noise. The trip 0.41c case shows an interesting effect. With respect to noise attenuation, it appears in this example qualitatively that the dilatation field in the trip 0.41c case has weaker (+/-) acoustic propagation. The flow field plots have shown clearly that the location of the trip can have dramatic effects on the flow field, visually illustrating the relationship between the flow field and the aeroacoustics data. The next step would be to take a closer look at the acoustics via unsteady pressure signals.

After the CFD reached steady state, it was possible to begin to observe the acoustics within the flow field data. The dilatation field, Figure 3.9, and the pressure field were early indicators of the acoustic wave information within the data. Therefore, by way of calculating the unsteady sound pressure signal one can determine the presence of acoustics within a pressure field, $p'(t) = p(t) - \bar{p}$. Here $p'(t)$ is the unsteady pressure signal, or the fluctuating sound pressure, p is the pressure as a function of time, and \bar{p} is the temporal average. The pressure field can also be visualized. Figure 3.9 shows the wave fronts, and corresponding sources. According to the data, it appears that the TE is the most dominant noise source, the near wake second most dominant, followed by the LE, and the TBL, Figure 3.10:

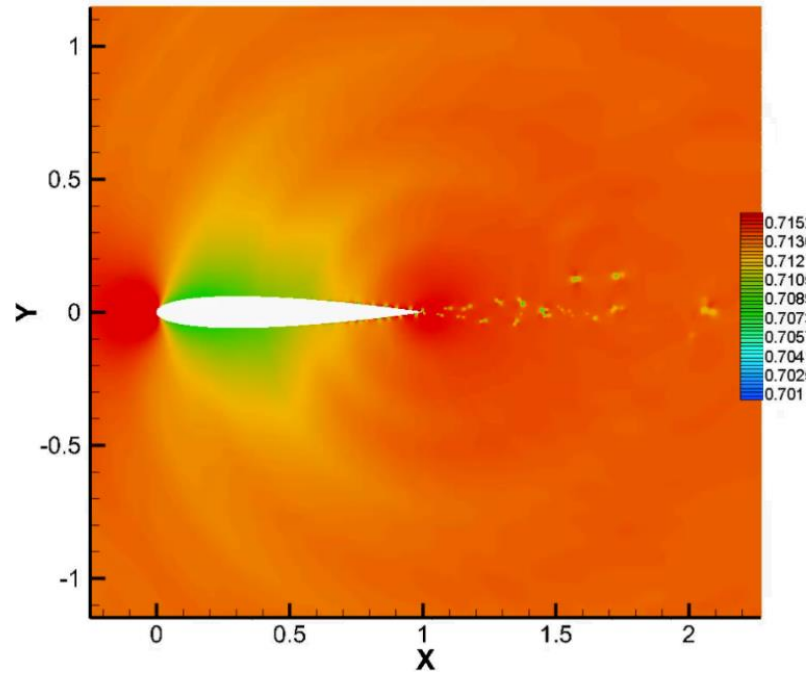


Figure 3.10 Instantaneous 2D Baseline case, pressure field with acoustic waves.

It is also possible to probe the solution file for pressure signals which was implemented for this study. To verify the CFD data juxtaposed to the BANC experimental data, it was necessary to quantify the far-field, and directivity patterns as defined in the workshop. The following figure illustrates the data acquisition locations, 1-point SS and 1-point PS at $r = 2.5c$, 90° orthogonal to the TE for the far-field, and 360 points (one per degree) at a radius of 1-meter, or $r = 2.5c$ for the directivity, Figure 3.11:

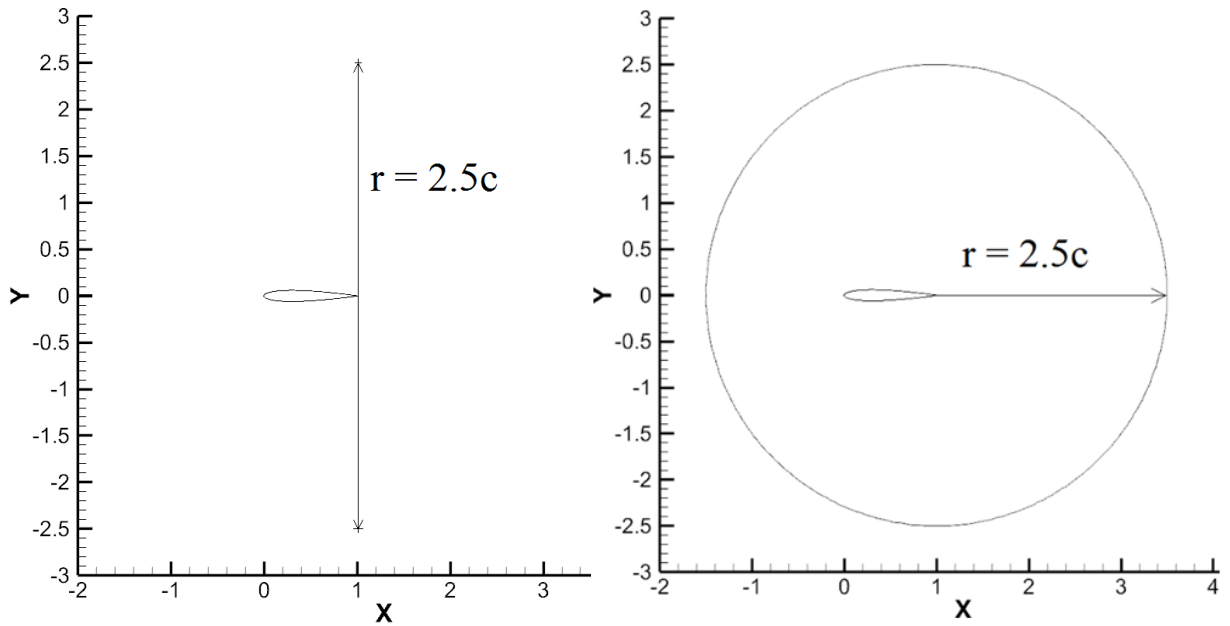


Figure 3.11 Acoustic field data extraction locations far-field (left), directivity (right).

To compare with the BANC acoustic data, the pressure signal needed to be post-processed in one-third octave band analysis. The method begins with the decomposition of $p'(t)$ into its frequency components using a fast Fourier transform (FFT) decomposition which yields the power spectral density (Delfs, 2009). The mean of the absolute value of this FFT breaks it down into its frequency components. The symmetric half of the power spectral density is then removed, and that of the frequency space. For our case, the 16,384 samples that were collected, generated every 44 iterations, in the end become 8,192 observable samples. For characterization of aeroacoustics noise with spectral peaks this would be the final step plotting the narrow band spectra, with $\Delta f = 2.1 \text{ Hz}$, against the frequency space, but for the one-third octave band analysis the data needs additional treatment to be further decomposed into bands. For the BANC workshop the center frequencies, 1 kHz, 2 kHz, 5 kHz, 8 kHz, and 10 kHz, of the one-third octave bands are standardized in EN ISO 266 as listed in Table 3.2:

Table 3.3: One-third octave bands standardized [Engineering Toolbox.com].

One-Third Octave bands		
Lower band limit, Hz	Center frequency, Hz	High band limit, Hz
891.0	1000.0	1122.0
1778.0	2000.0	2239.0
4467.0	5000.0	5656.0
7079.0	8000.0	8913.0
8913.0	10000.0	11220.0

At this point, all the data within the one-third octave bands about the center frequency were averaged into one value to represent the entire band, then the PS and SS retarded observer positions were accounted for in this BANC defined formula:

$$L_{p(1/3)} = 10 \log_{10} [10^{L_{p(1/3),SS}} + 10^{L_{p(1/3),PS}}] \quad (3.1)$$

For comparing the relevant far-field data this pressure signal decomposition was the last step, and for comparison the resulting data were plotted against the BANC Workshop numerical and experimental data. It is important to note that the far-field data presented herein have some differences in Aspect Ratio, velocity, and in some cases tripping location, and for this reason a table has been inset to the figure to communicate these discrepancies. Figure 3.12 shows the far-field one-third octave band TBL TE noise spectrum compared with the 2D data:

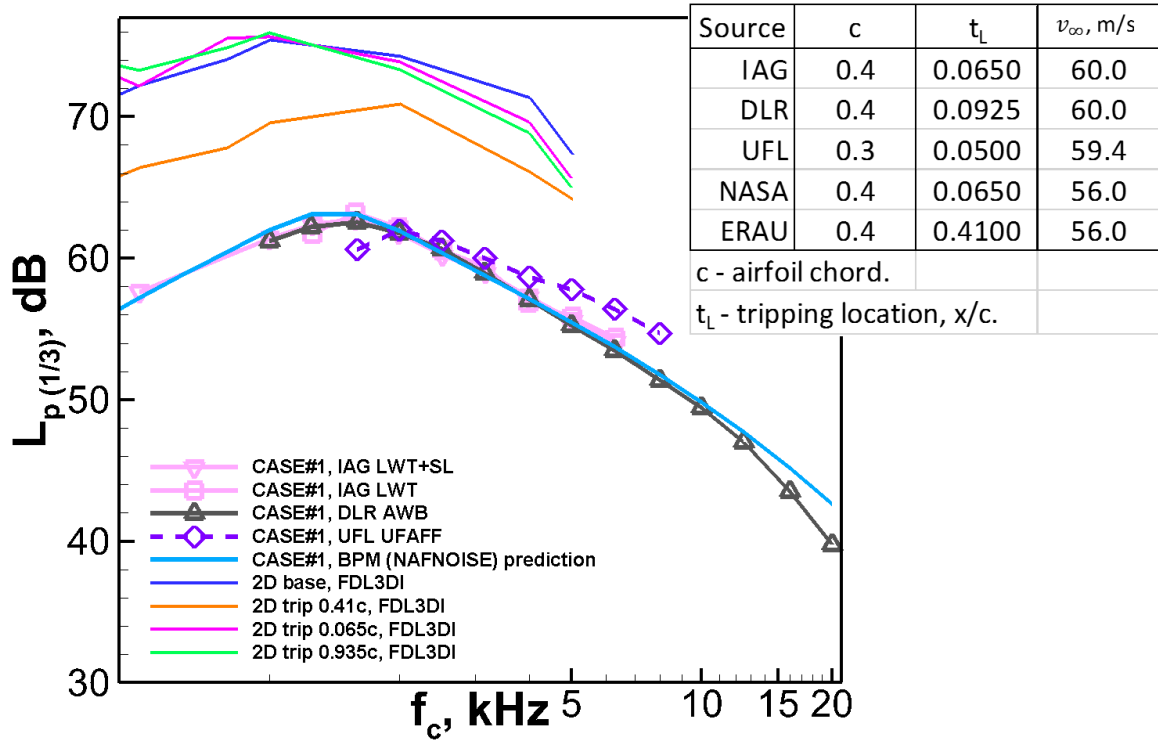


Figure 3.12 Far-field one-third octave band TBL-TE noise spectrum (re $2e-5$ Pa) with BANC data for comparison.

It was observed that up to a certain frequency the data trends fair reasonably, but then falls off. The cut-off frequency was determined by understanding the Nyquist frequency is half of the sampling rate of a discrete signal (Olshausen, 2000). If the time between samples is dt , then the highest resolvable frequency is defined as $f_n = 0.5/dt$. For the present study, $dt = 0.00009$, and therefore the highest resolvable frequency was calculated to be $f_{cut-off} = 5,555$ Hz. The spectra in Figures 3.12, and 3.13 do not present data above the cut-off frequency, and have corrected power density scaling (Bahr & Cattafesta, 2011).

For creating the directivity patterns to compare with the BANC Workshop data, one more step was needed past the one-third octave band treatment. First, each signal needed a root mean square (RMS) in time, normalized by a mean RMS in space, defined

by the BANC Workshop and presented here as:

$$p_{rms}(\theta)/\overline{p_{rms}(\theta)}, \quad \text{with } \overline{p_{rms}(\theta)} = \frac{1}{2\pi} \int_0^{2\pi} p_{rms}(\theta) d\theta \quad (3.2)$$

For radius $r = 1$ meter, or $r = 2.5c$, for one-third octave band center frequencies $f_c = 1 \text{ kHz}, 2 \text{ kHz}$ and 5 kHz the spacing was $\Delta\theta = 1^\circ$, or for each pressure signal one per degree separation in a defined circle about the TE. The directivity patterns show the dominant direction of the pressure waves, Figure 3.13:

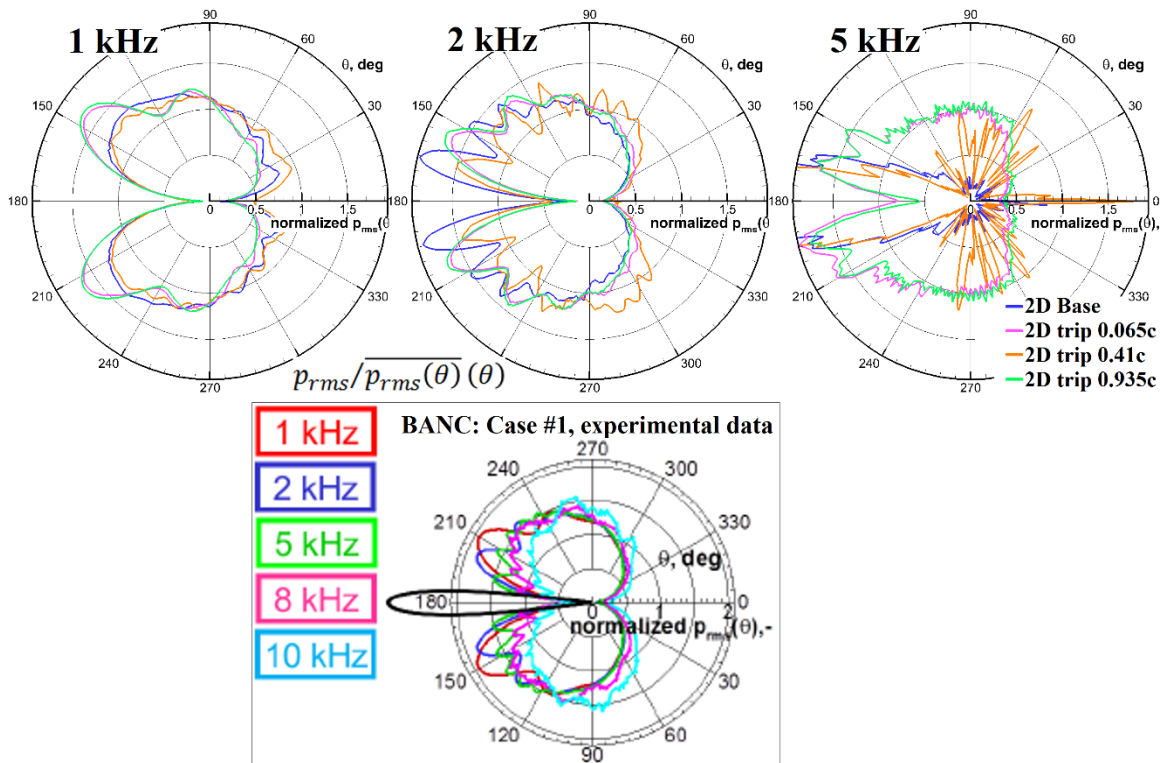


Figure 3.13 2 Far-field 1/3-octave band TBL-TE noise directivity patterns $p_{rms}(\theta)/\overline{p_{rms}(\theta)}$, from top CFD data, bottom BANC comparison data for Case 1.

The first observation is that all of the data above the 5,555 kHz cut-off frequency has been neglected. Secondly, with respect to comparison with the BANC Workshop the CFD data trends are comparable.

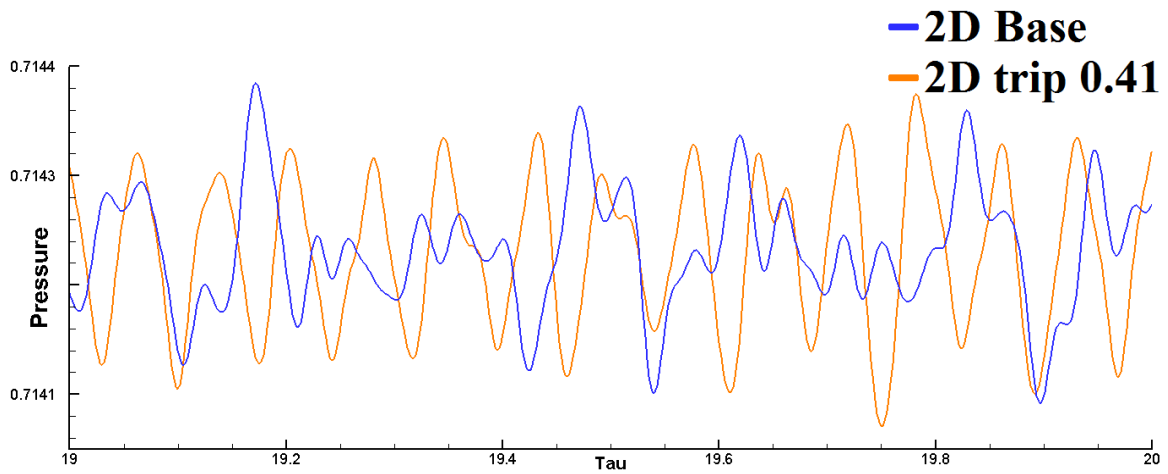


Figure 3.14 Pressure time history for pressure probe located at station $(x, y) = (1, 2.5)$ for 2D duration non-dimensional time $\text{Tau} = 19$ to 20 .

The time trace of the pressure signal in Figure 3.14 is consistent with some features of the spectra shown in Figure 3.12, but also raises some issues. The untripped case seems to consist of a dominant large-amplitude low-frequency one (large periods), and some weaker high frequency ones (smaller periods), but they are not well organized. When tripped, this trace is replaced with a well-organized one that seems to be essentially a narrow frequency band. For this reason, this trace is consistent with the overall drop in the corresponding spectra. However, both the clean and the tripped traces indicate the existence of peak frequencies none of which showed up in the corresponding spectra. This leads us to believe that the FFT scheme adopted here tends to smooth out the spectra, but it is not capable of detecting peaks at narrow frequencies or tones. In other words, the spectra presented here may be correct as average, but it fails to predict sharp peaks.

The 2D data in the far-field appears to over-predict the TE noise by about 8-10 dB, which is expected since this is 2D simulations. The directivity patterns in the lower center frequencies compare well to the BANC Workshop data and consistent with the literature

which communicates the TE as a noise source appearing as an oscillatory dipole just downstream (Tam, 2012).

Observing the far-field data, the tripped 0.41c case appears to have lower levels predicted in the lower frequencies by about 4-8 dBs across all frequencies above the cut-off frequency. This data is consistent with the lower levels of dilatation observed earlier in Figure 3.9 that appear to show the 0.41c tripped case has smaller amplitude waves. The data was surprising but was at least consistent with the literature that tripping the BL may attenuate one or more of the TE noise mechanisms (Brooks et al., 1989). We need to reiterate, however, that this is a 2D simulation, which is limited to capturing only the 2D large scale structures, and not the physical 3D turbulent flow. However, this data helps guide us in starting our realistic simulations in the next section.

4. Three Dimensional Results

4.1 Grid and Boundary Conditions

To facilitate the export from Pointwise, and the corresponding import into Pegasus and BELLERO, the baseline grid was broken into three blocks, with 11-point overlap on the SS, and the PS at about 0.51c, and a 5-point overlap at the LE. The extensive overlap was to avoid interpolation errors with the flow solver, and the location of the grid decomposition into blocks was such that the overlap would be farthest from the TE location of interest. The 3D study focused on the most interesting 2D case, trip 0.41c, and the Baseline case for clarity, and conciseness. The trip 0.41c grid was decomposed as before, with a LE block, a TE section, and SS and PS trip blocks, as illustrated in Figure 4.1:

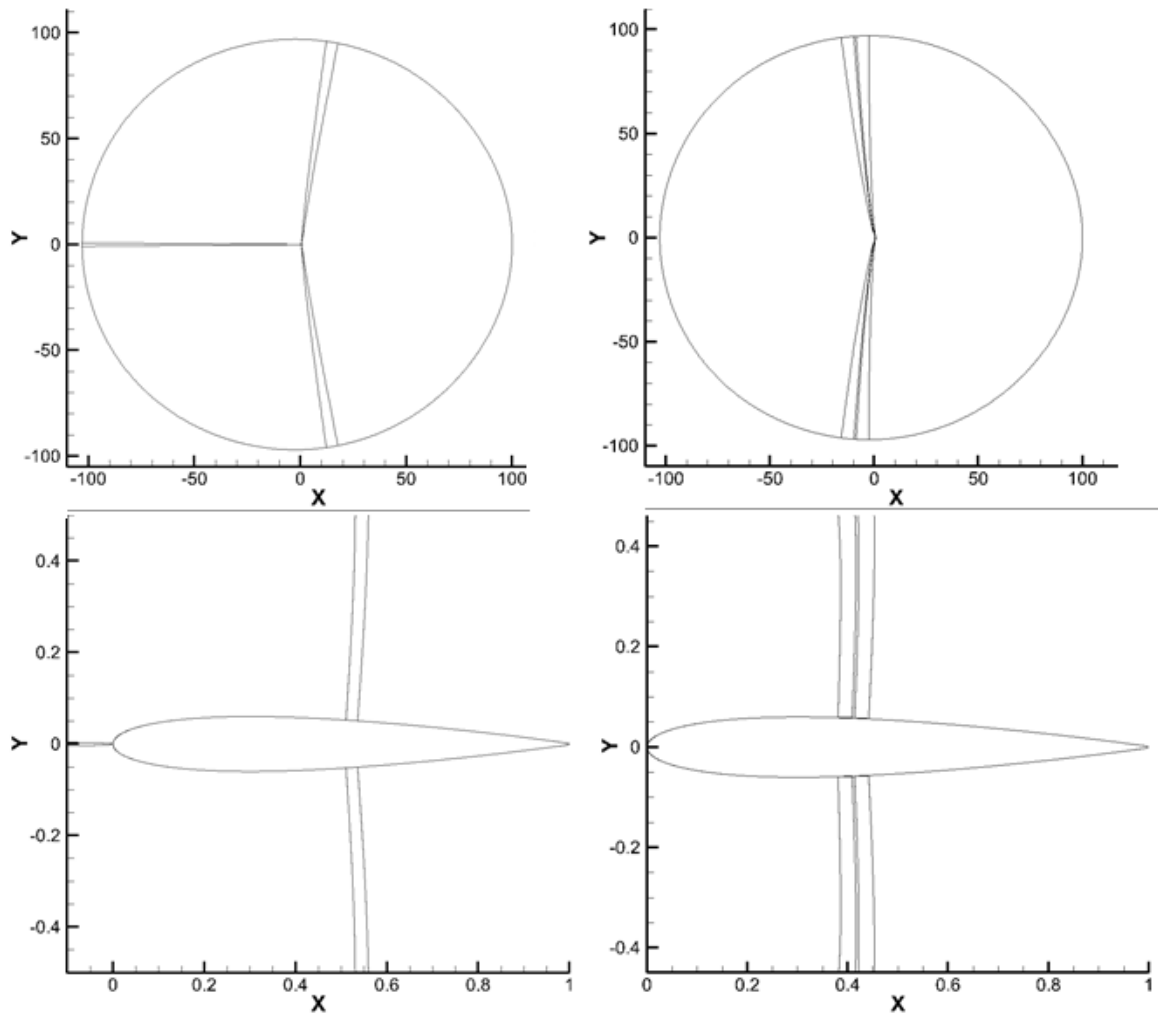


Figure 4.1 The 2D and 3D baseline (left), and trip 0.41c (right), whole grid (top), and close-up of airfoil-mesh region showing block overlap region (bottom), respectively.

Careful attention to detail was used to determine the grid spacing to maintain the $y^+ < 1$ recommended by LES recommendations and practices, and to choose the correct z^+ for the 3-dimensional grid. According to Georgiadis et al., 2010, 157-points in z would be recommended for LES $z^+ < 40$, however, 101-points was agreed upon by ERAU's CAA group. Table 4.1 shows the Baseline and trip 0.41c grid breakdown:

Table 4.1 1 NACA-0012 grids employed in 3D studies.

Cases	#blks	Dimension	$\Delta x/c$	$\Delta y/c$	$\Delta z/c$
3D Base	blk-1	371x1577x101	2.50E-03	1.25E-05	1.00E-03
	blk-2	371x1577x101	2.50E-03	1.25E-05	1.00E-03
	blk-3	561x1577x101	2.50E-03	1.25E-05	1.00E-03
3D Trip	blk-1	25x1508x101	2.50E-03	1.25E-05	1.00E-03
	blk-2	25x1508x101	2.50E-03	1.25E-05	1.00E-03
	blk-3	637x1577x101	2.50E-03	1.25E-05	1.00E-03
	blk-4	637x1577x101	2.50E-03	1.25E-05	1.00E-03

The boundary conditions remained the same as the 2D studies previously mentioned in Table 3.1.

4.2 Snap shots of the flow & acoustic field tripping vs. clean

It is useful to generate instantaneous plots of the pressure field, and dilatation field, to capture acoustic waves and provide a qualitative feel for the behavior of the acoustics as they propagate within the flow field. Which are shown here in Figure 4.2. The 3D dilatation field shows that tripping has affected the location of transition, but no TEN attenuations. For the 2D acoustic far field, as outlined before, appears to be attenuated showing diminished (+/-) for the tripped case, but is not physical.

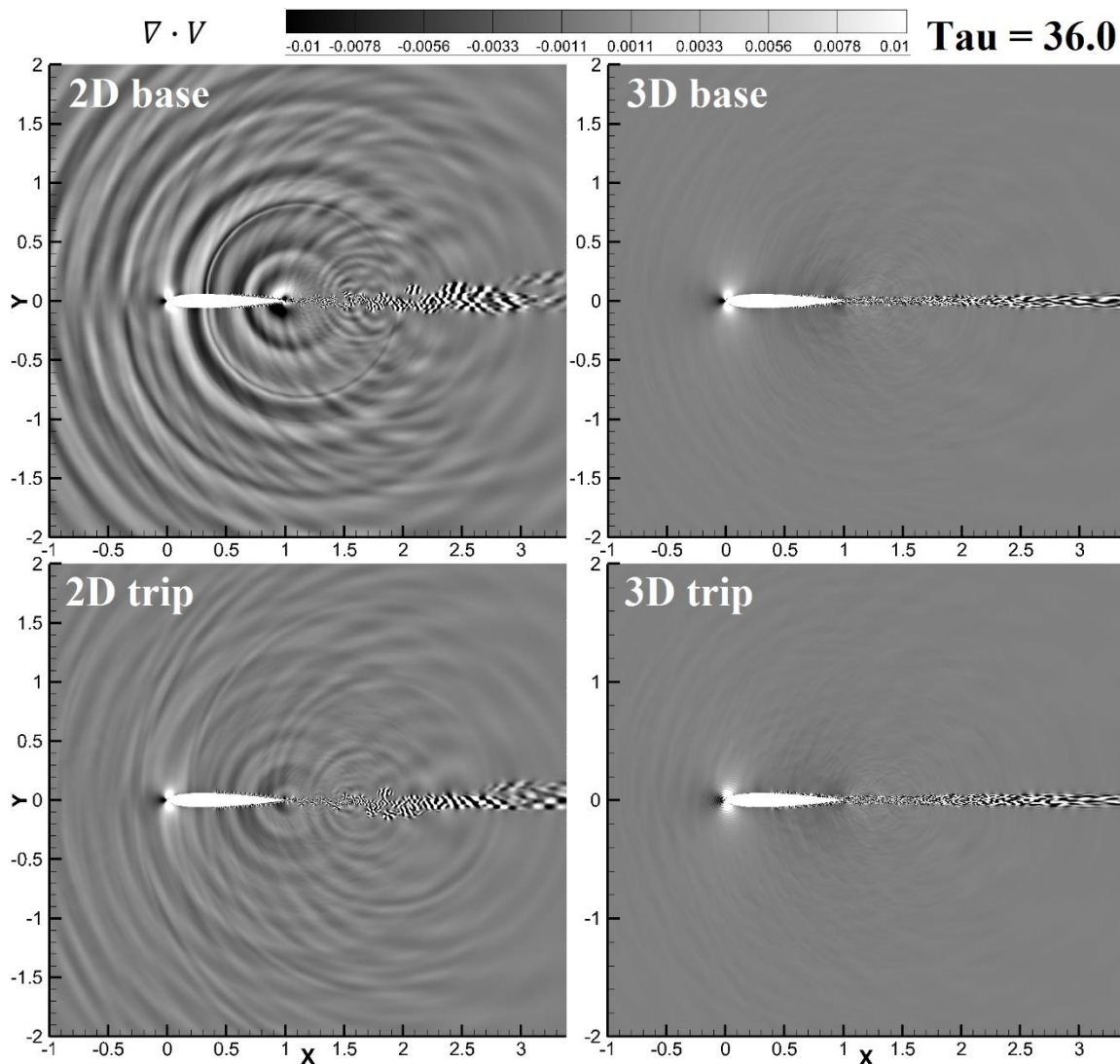


Figure 4.2 Instantaneous dilatation field at $\tau = 36$ for 2D (left), and 3D (right) plots for the baseline (top) and trip 0.41c (bottom) cases, respectively.

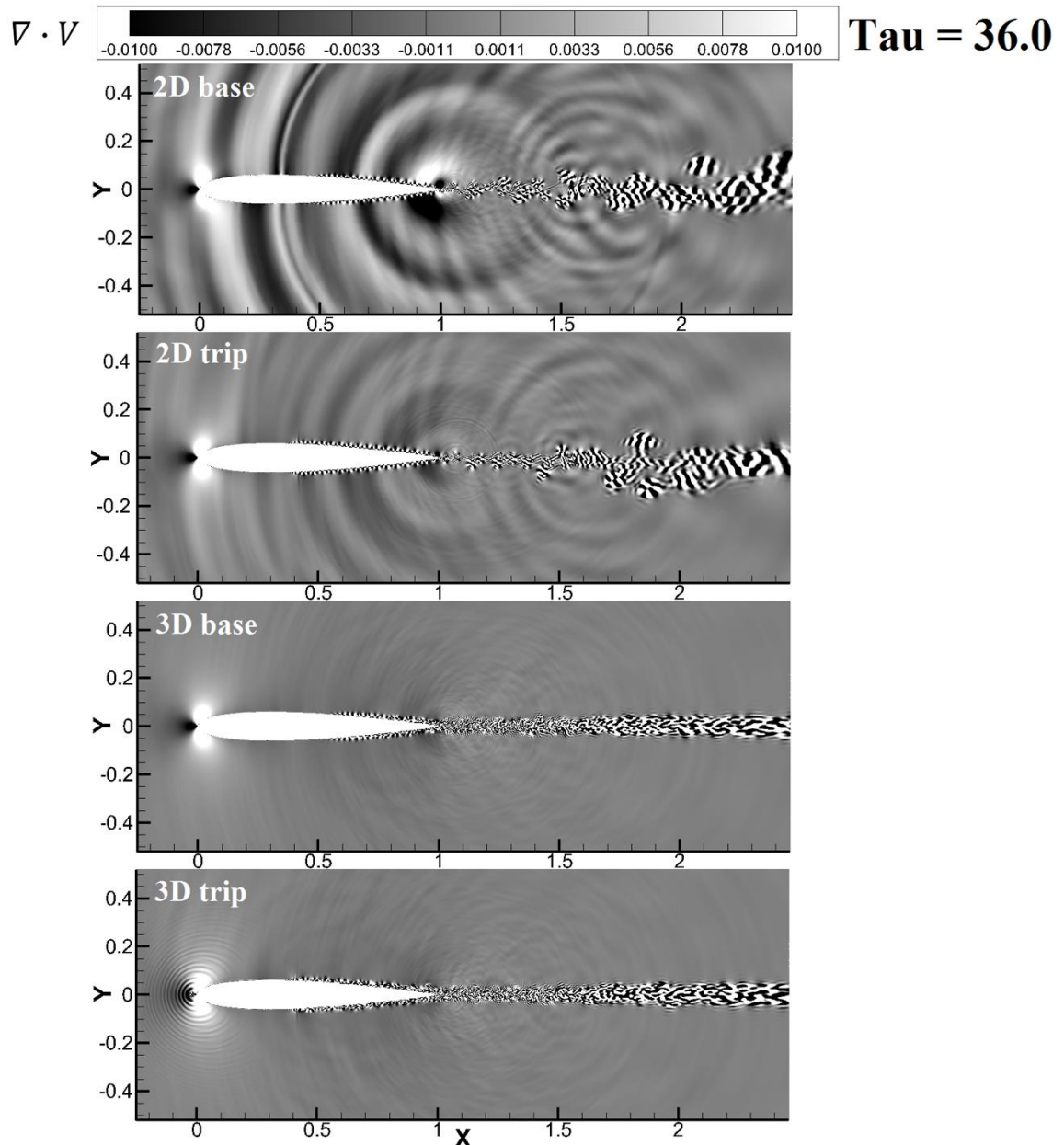


Figure 4.3 Instantaneous dilatation field plots at $\tau = 36$ for 2D (top two) and 3D (bottom two) baseline (first, third) and trip 0.41c (second, fourth) cases, respectively.

Figure 4.3 shows a closer look at the dilatation: or the 3D data, pressure field plots were generated, but the effect of tripping was not pronounced. The greatest distinguishable feature between the two 3D cases with respect to the pressure exists in the surface pressure data, which will be examined later. Figure 4.4 shows the instantaneous pressure contours:

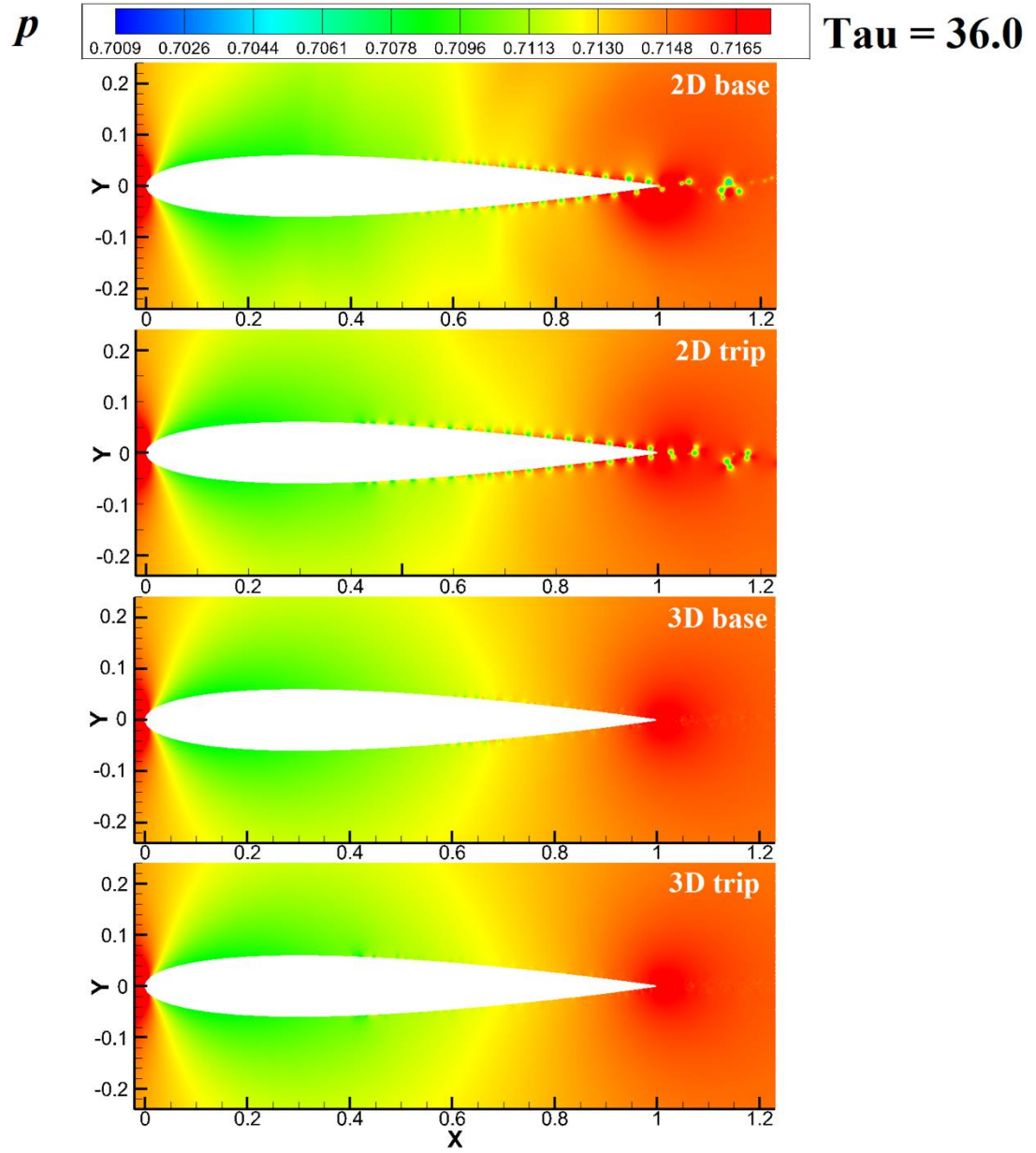


Figure 4.4 Instantaneous pressure field plots at $\tau = 36$ for 2D (top two) and 3D (bottom two) baseline (first, third) and trip 0.41c (second, fourth) cases, respectively.

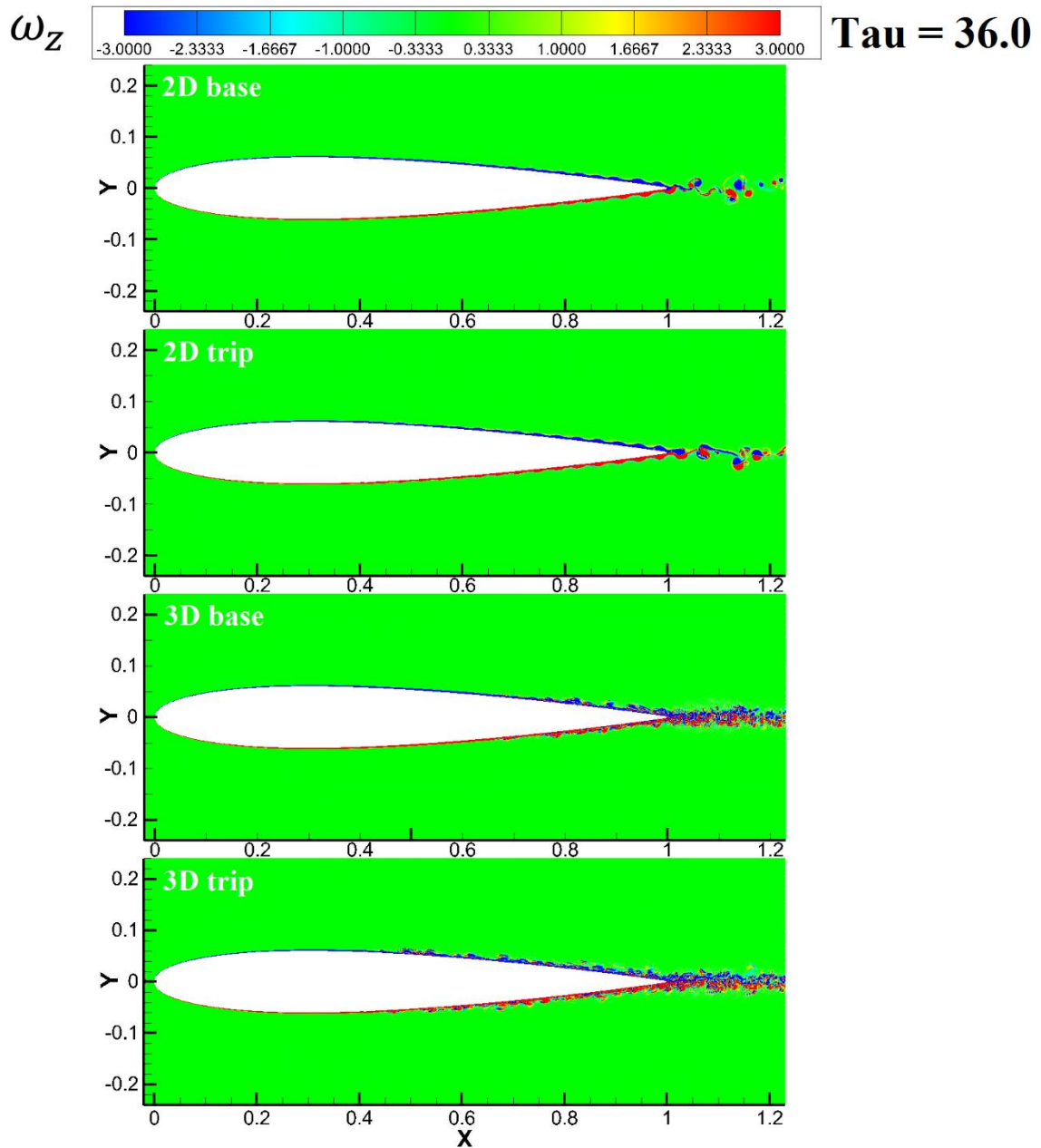


Figure 4.5 Instantaneous z-vorticity field plots at $\tau = 36$ for 2D (top two) and 3D (bottom two) baseline (first, third) and trip 0.41c (second, fourth) cases, respectively.

Figure 4.5 shows snapshots of the vorticity. For the 3D case, tripping leads to earlier transition compared to the not tripped case. The vortex shedding seems to be absent in the 3D case as compared to the 2D case.

4.3 The Sound Sources

This section focuses the study on the relevant noise mechanisms witnessed based on observation, TBL-TE noise, LBL-VS noise, and TEB-VS noise.

4.3.1 Flow over the Airfoil Surface

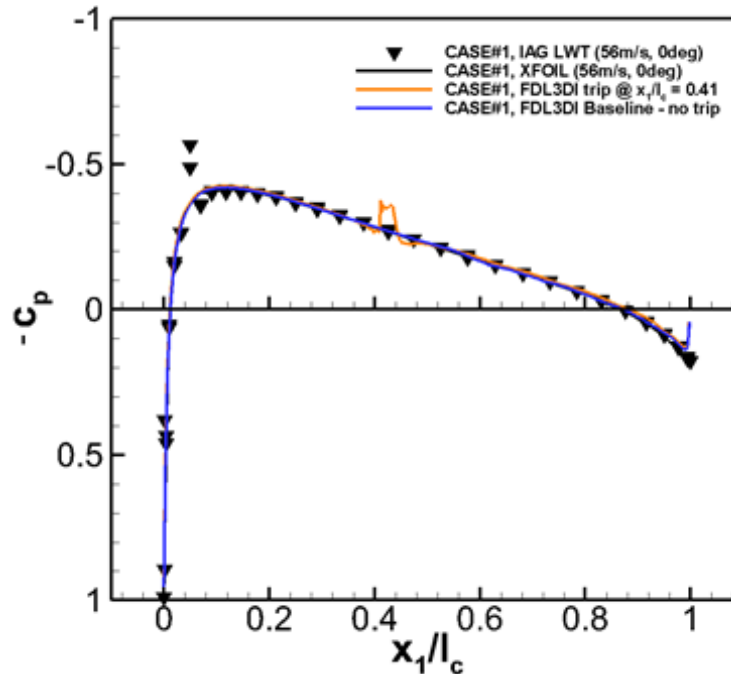


Figure 4.6 Mean pressure coefficient for the 3D baseline case, trip 0.41c case, and experimental data.

Since transition to turbulence is itself a known acoustic source and knowing where transition occurs is of vital importance to this study, the skin-friction coefficient would also need to be determined. Figure 4.6 shows the mean pressure coefficient: Both 3D cases show similar pressure distribution except in the region of the trip, and comparable to the experimental data. The spike in pressure on the tripped surface may indicate the beginning of a BL instability.

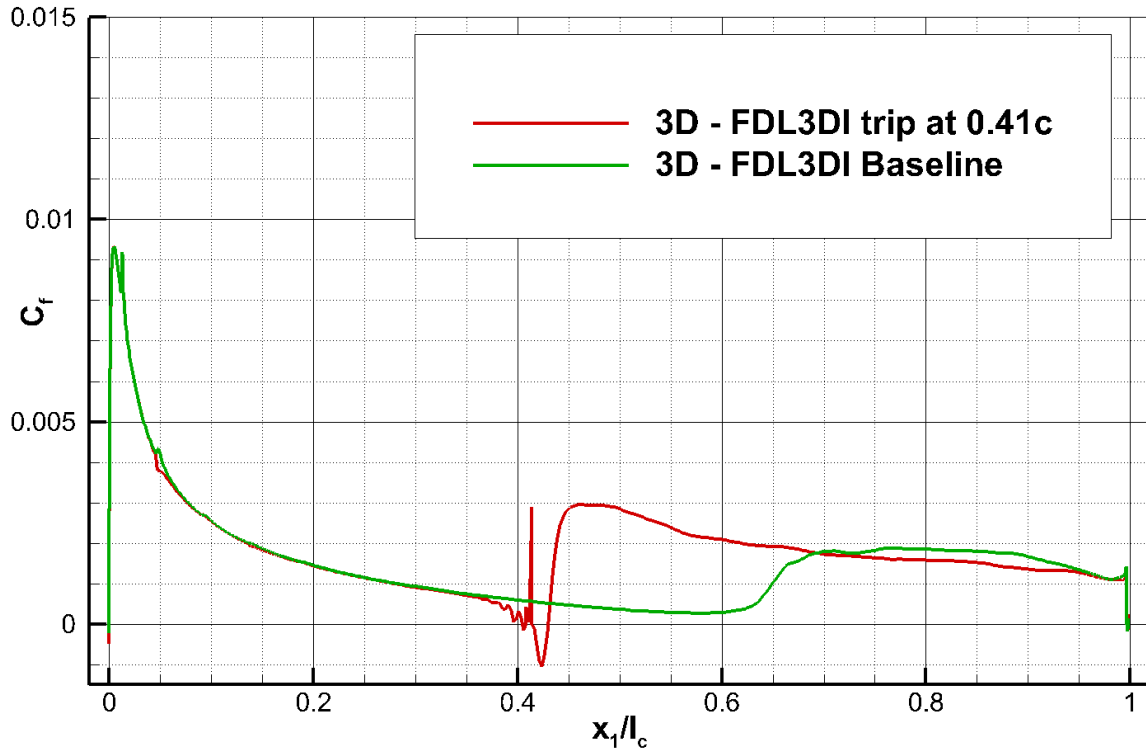


Figure 4.7 3D mean skin friction coefficient comparing the baseline, and trip cases.

When analyzing the TBL, perhaps the most important characteristic is the wall shear stress. Figure 4.7 examines the mean skin friction coefficient which is a measure of the wall shear stress. For the tripped case, the mean skin friction coefficient shows a small separation region (crosses zero) on the airfoil surface. The rapid growth indicates transition, followed by re-attachment as a TBL. Separation, reattachment, and transition are all unsteady events that lead to instability waves (Mankbadi, 1994). It can also be seen that compared to the baseline case, the skin friction is stronger in the turbulent region after being tripped. For the baseline case, the BL never separates however there is a rapid growth after 60-percent chord indicating a transition from laminar to TBL.

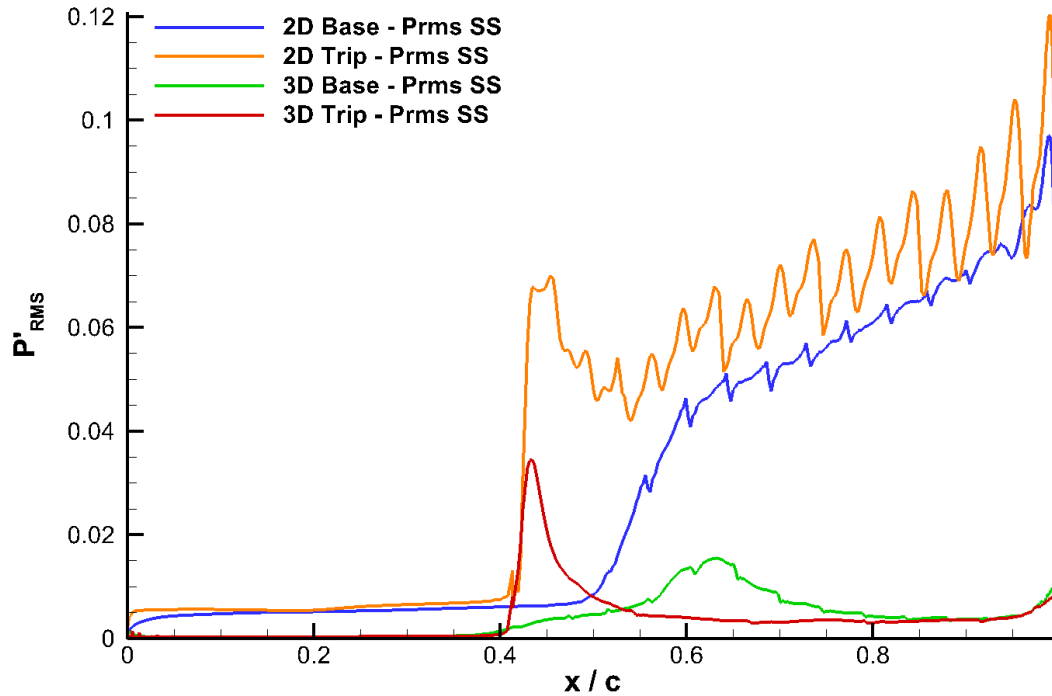


Figure 4.8 P'_{rms} on the SS of the airfoil for the baseline, and trip 0.41c cases.

The root-mean-square (rms) of the unsteady pressure on the airfoil surface was extracted for 1,024-time steps to be analyzed. Figure 4.8 shows the tripped and un-tripped cases: Clearly it can be perceived from the 3D data that tripping initiates an instability wave within the pressure on the airfoil surface. The baseline case transitions rapidly after mid-chord, however does not reach the level of the tripped surface RMS pressure. The 3D data illuminates the initial instability spike for the tripped case, and the gradual instability growth.

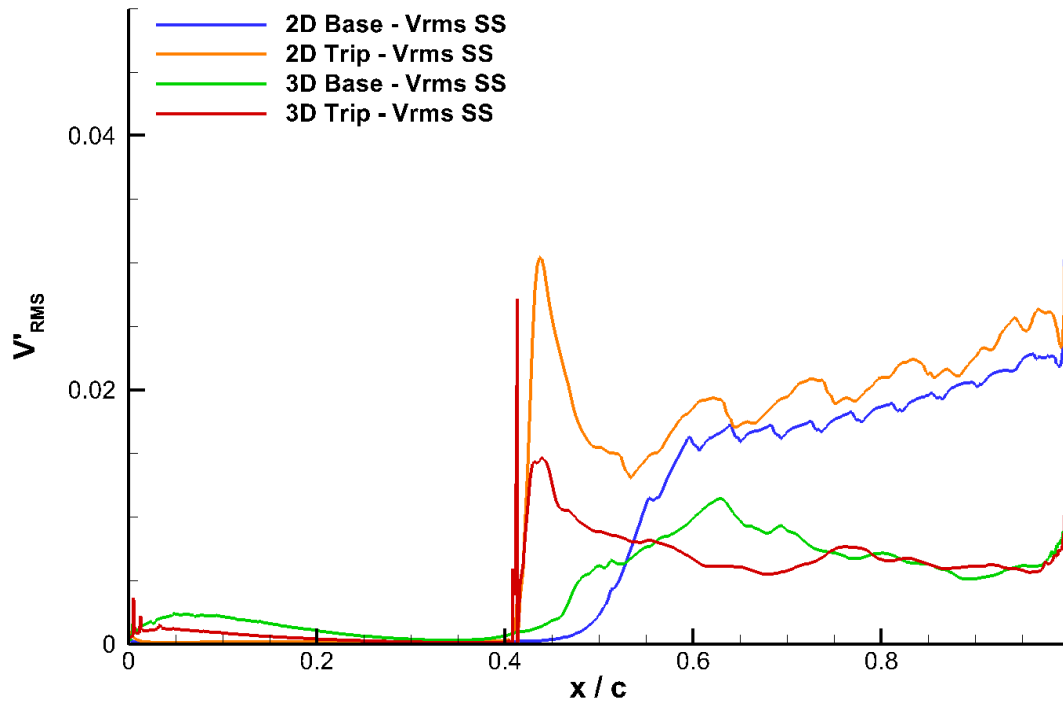


Figure 4.9 Fluctuations in tangential velocity for Baseline, and trip 0.41c cases on the airfoil surface.

The fluctuations in the tangential velocity can also show the presence of instability waves. The rms of the fluctuations in u-velocity on the airfoil surface are shown in Figure 4.9: The same trend as the 3D fluctuating pressure signal appears in the unsteady tangential velocity data around mid-chord. The trip triggers a steep climb of V'_{rms} in both the 2D and the 3D data, initiating an instability wave that persists within the TBL for the remainder of the airfoil surface flow. The baseline case shows the inflection of natural transition from a steady laminar BL to a fully TBL after about mid-chord. The 2D tripped V'_{rms} appears stronger than the baseline case toward the TE of the airfoil, but the 3D data does not substantiate this behavior.

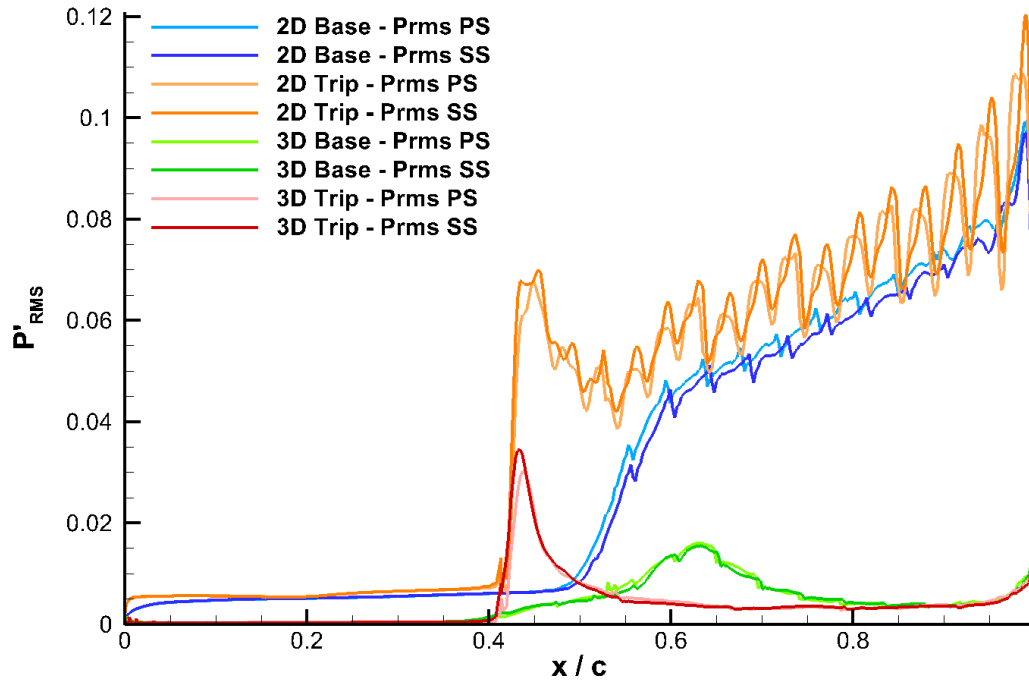


Figure 4.10 P'_{RMS} on the SS and PS of the airfoil for the Baseline, and trip $0.41c$ cases.

To further elucidate how artificial tripping of the BL forces the TBL into symmetrical behavior the SS and PS fluctuations of pressure and velocity of the two cases were extracted and plotted together, Figure 4.10: The 3D data pressure fluctuations for both cases are very symmetric SS and PS, very similar in magnitude, and nearly identical in phase. They also appear to be very similar in magnitude for the last 10 percent of the airfoil surface. For the 2D clean case there seems to be some phase shift for the fluctuation on the PS vs SS. However, this shift seems to disappear for the 2D tripped case.

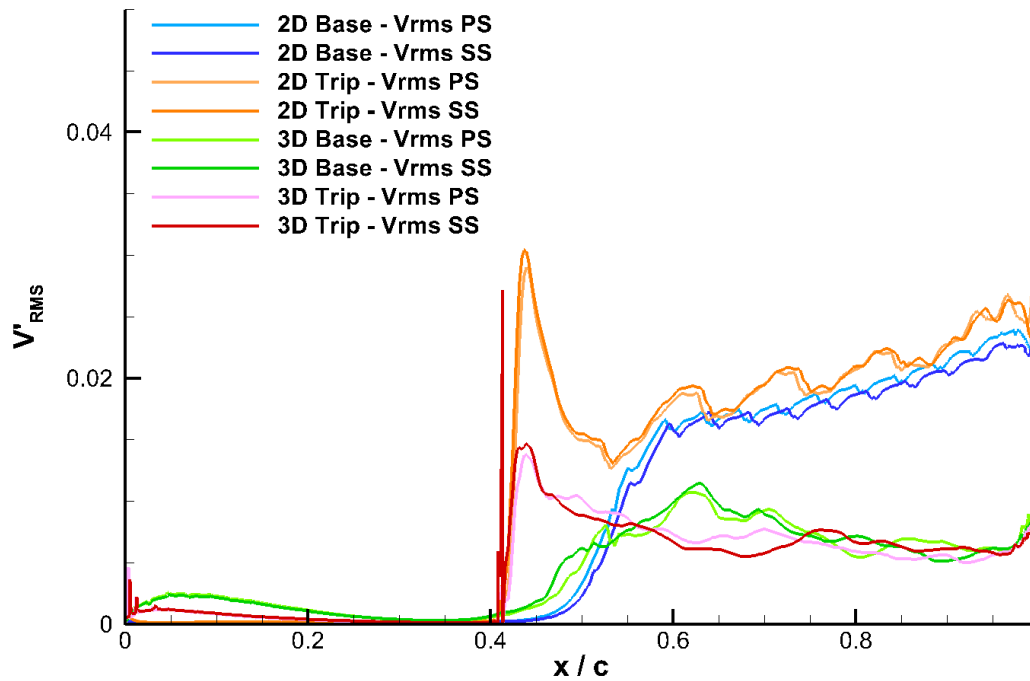


Figure 4.11 V'_{rms} on the SS and PS of the airfoil for the Baseline, and trip 0.41c cases.

For the sake of completeness, the SS and PS tangential surface velocity of the two cases were also analyzed. Figure 4.11 displays the results: For the 3D case, there seems to be no phase shift between the PS and SS in the velocity fluctuations. For the 2D case there seems to be some phase shift of the velocity fluctuations between the PS & SS near the TE.

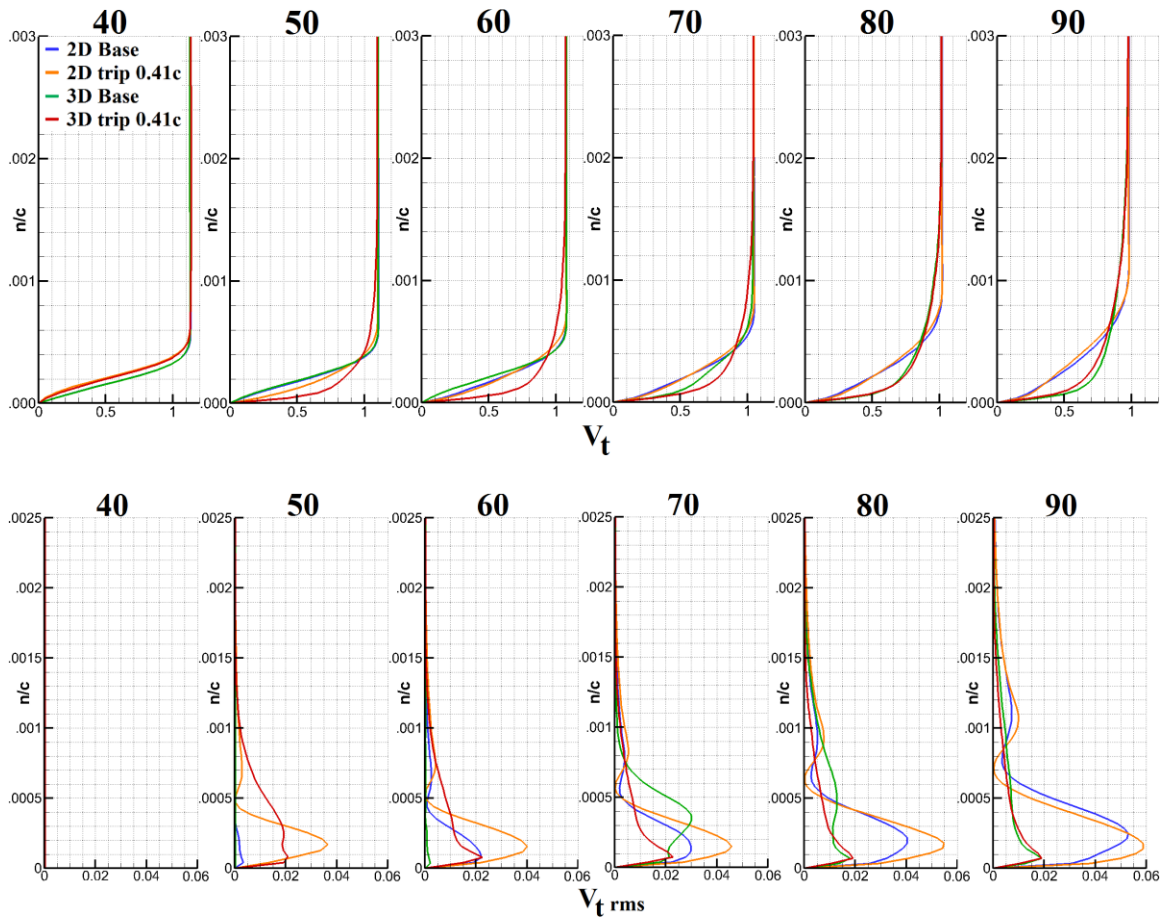


Figure 4.12 Comparison of 2D base (blue) and trip (orange) vs. 3D base (green) and trip (red) cases, respectively, SS boundary-layer profiles. Top) Averaged tangential U-velocity, Bottom) $U_{t,rms}$ -velocity.

Boundary layer analysis is given in Figure 4.12. From the mean velocity profiles, the 3D tripped case's BL is fully turbulent at station 50. It is also clear that the baseline case transitions about 60 percent chord, and becomes fully turbulent to be even thicker than the tripped case at station 90. We note that the 3D profile is fuller in the 3D case compared to that of the 2D case. We also note that for the 2D case the difference of the fluctuations level between the tripped and clean persists to the TE.

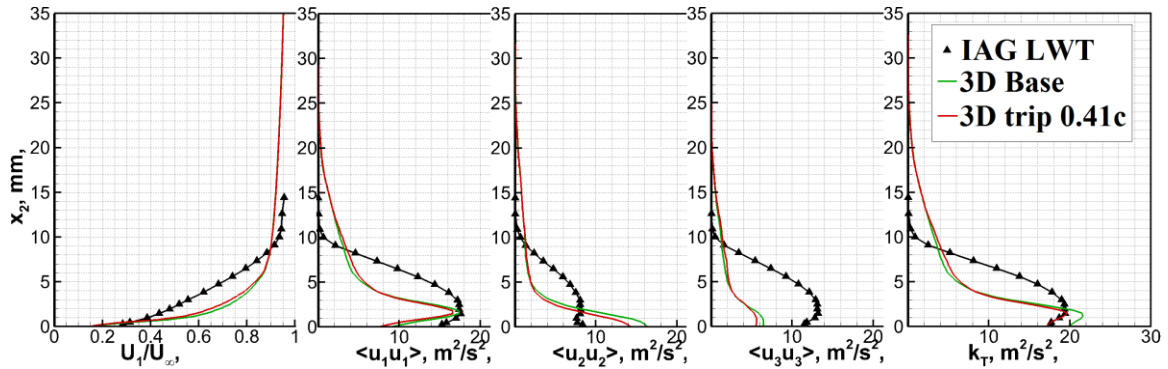


Figure 4.13 3 The 3D mean velocity profile u/u_∞ , and the mean fluctuating components of velocity $(\overline{u'u'})$, $(\overline{v'v'})$, $(\overline{w'w'})$, and TKE are taken at $1.0038c$ for both cases.

We compare in Figure 4.13 our 3D results for the boundary characteristics right after the TE to the experimental one. The two compare well, but in our predictions the mean flow seems to be fuller than that of the experiment, and the Reynolds stresses are concentrated in a smaller y -region near the wall. It is not clear whether this can be attributed to the fact that the spanwise length in this simulation, 0.1 , is smaller than that of the experiment, 1 . According to the TKE in Figure 4.13 it appears in the baseline case, the turbulence in the immediate wake after the TE is 10 - 15% stronger than the tripped case.

4.3.2 Spectral Analysis

To observe the existence of the frequencies introduced, one would need to analyze the spectral content of the pressure in the region very close to the airfoil surface. The effect of tripping may have introduced frequencies that changed the spectra. The downstream face of the trip is like a back-wards facing step. When the flow convects past it transition is immediate and the resulting acoustic field is effected immediately. For this study probes needed to be placed on the surface of the airfoil, at the $j = 1$ location of the grid, to measure

the pressure within the BL flow. The immediate region aft the trip in the chord-wise direction was selected as it was believed this would be a region of the flow directly affected by whatever frequency was introduced by the trip.

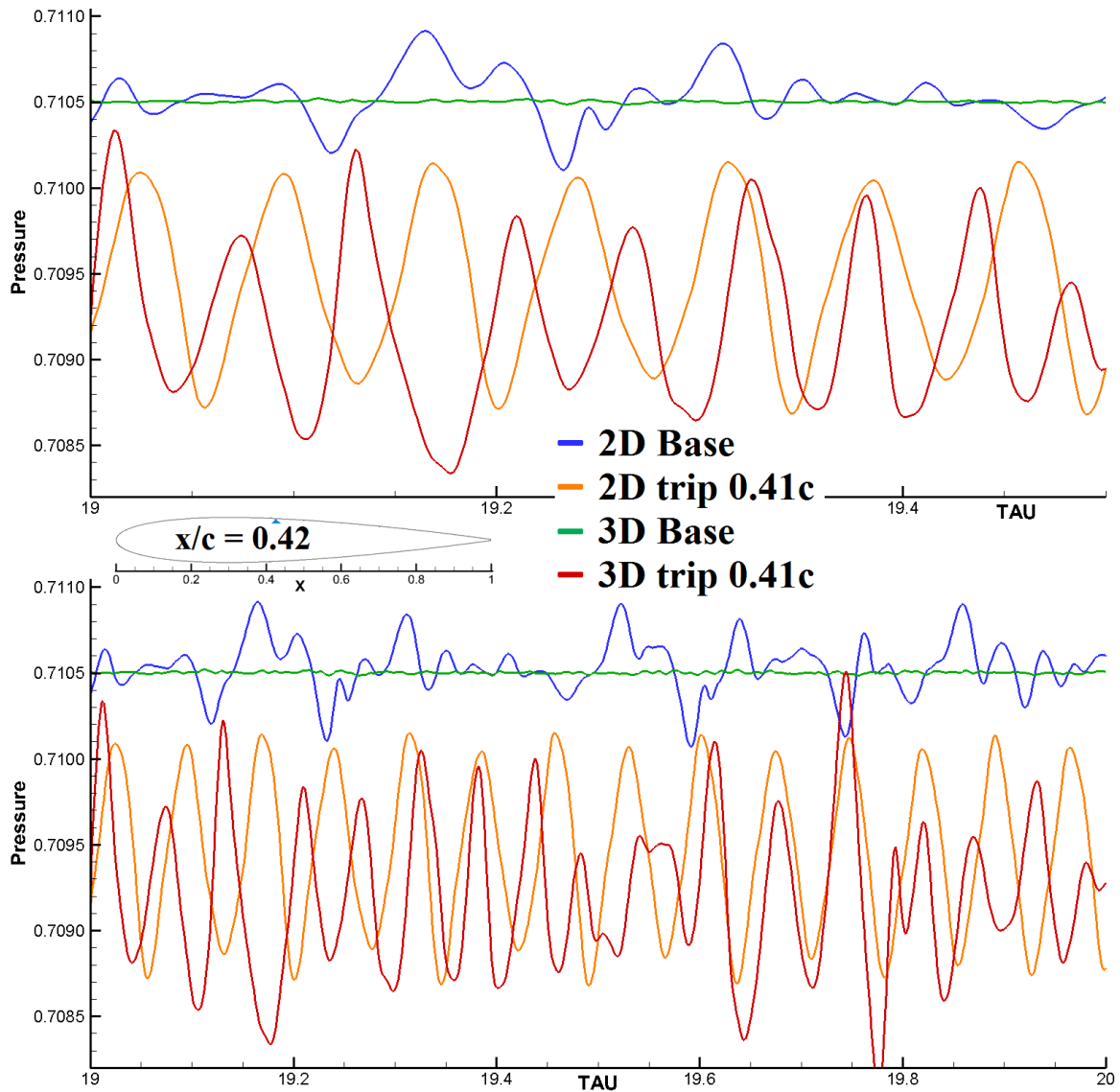


Figure 4.14 2D and 3D pressure time histories for pressure probe located at station $x/c = 0.42$ for duration non-dimensional time $\text{Tau} = 19$ to 19.5 (top), and $\text{Tau} = 19$ to 20 (bottom).

A comparison of the time trace of the pressure signals was investigated, Figure 4.14: The data presented in Figure 4.14 is from a suction side probe positioned in the flow volume

on the airfoil surface, at 42 percent chord in the region just aft the trip. As anticipated the 2D and 3D tripped cases shows greater amplitudes, but an overall lower pressure value. The greater amplitude is consistent with the higher levels in Figure 4.16. Observing pressure signals taken at station 98.9 percent chord, Figure 4.15:

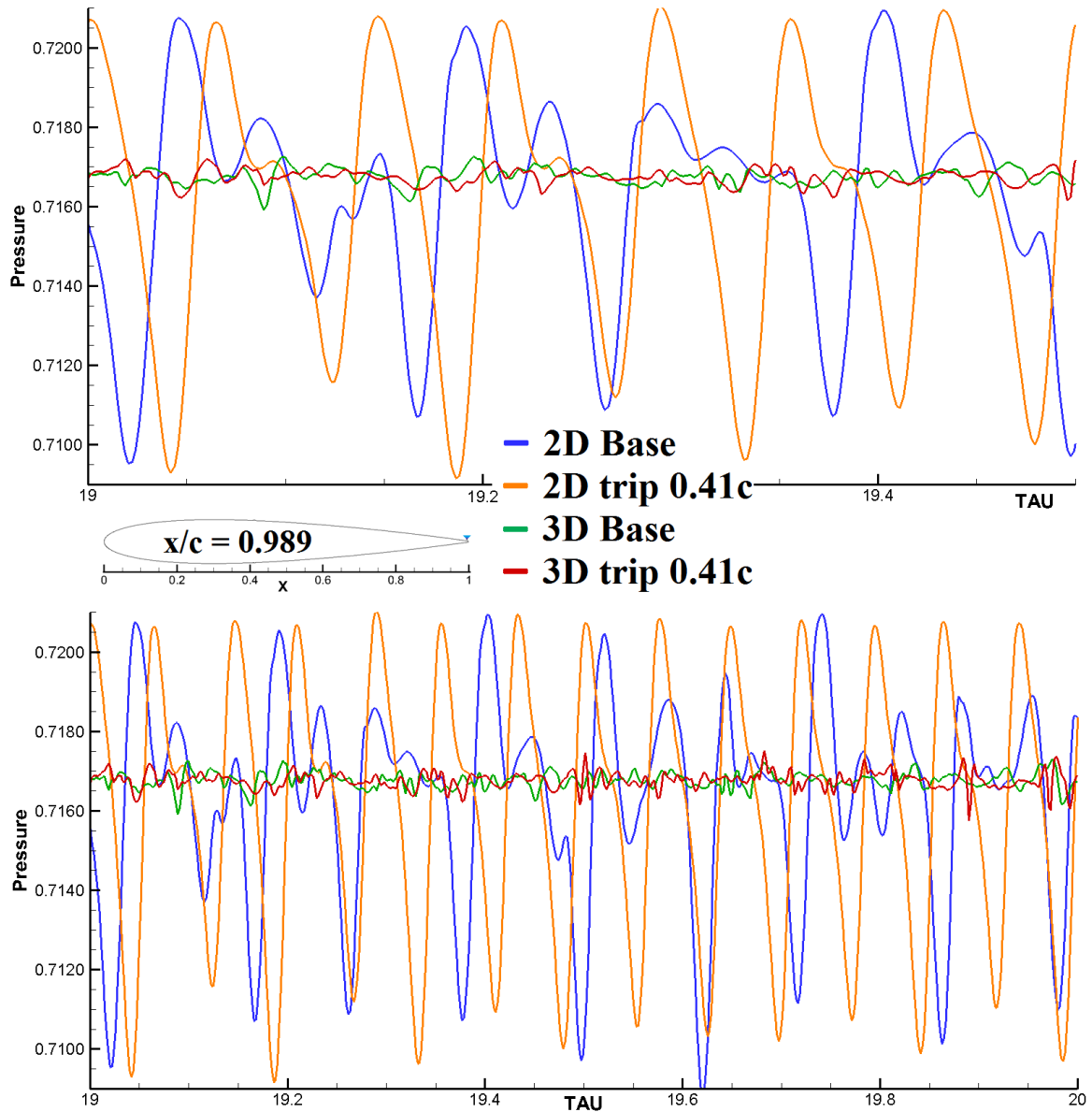


Figure 4.15 2D and 3D pressure time histories for pressure probe located at station $x/c = 0.989$ for duration non-dimensional time $\tau = 19$ to 19.5 (top), and $\tau = 19$ to 20 (bottom).

The time trace of the signal near the TE is shown in Figure 4.15. It is interesting to note that for the 3D data, the tripped and baseline signals appear very similar in level at this station which may indicate similar BL fluctuations at the TE. The surface pressure was measured on both sides of the airfoil, but only the SS data is presented herein for clarity as the two sides were similar.

For performing FFT, the airfoil surface pressure was measured to acquire 16,384 samples. An FFT of the pressure signal was undertaken decomposing it into its frequency components obtaining the power spectral density, with $\Delta f = 2.37$ Hz, the symmetric half discarded to produce the narrow band spectra presented in Figure 4.16. This same signal was further conditioned to decompose into the one-third octave bands that have previously been discussed. For the matter of the surface spectral content and being concise both methods were employed together, Figure 4.16. The locations of the probes are shown in Figure 4.18. The figure shows that tripping increases the pressure fluctuations at the surfaces, but this increase tends to diminish downstream. The tripping-introduced frequencies seems to be centered around 2 KHz, and no tones are introduced.

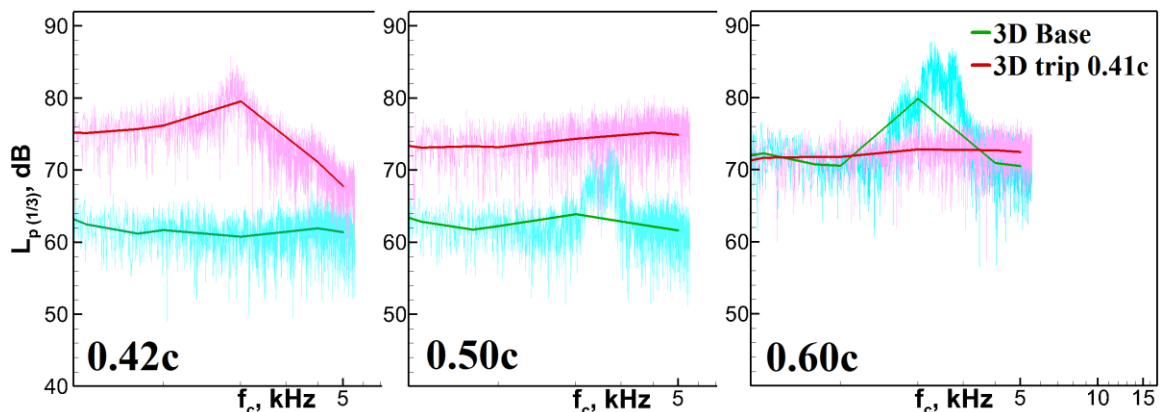


Figure 4.16 Narrow band PSD of the airfoil SS surface pressure at $x/c = 0.42$ (left), $x/c = 0.50$ (middle), $x/c = 0.60$ (left), over-laid with one-third octave band data at the same locations.

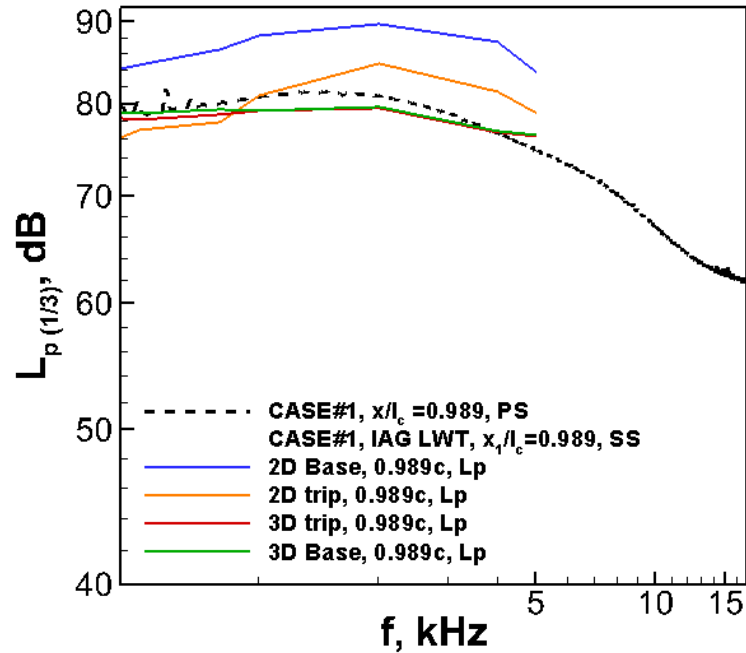


Figure 4.17 One-third octave band power spectral density at $x/c = 0.989$ compared with experimental data (Herr, 2016).

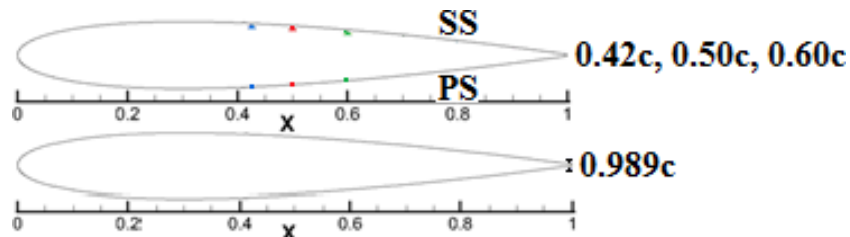


Figure 4.18 Suction side (SS) and pressure side (PS) pressure probe locations on the surface of the airfoil at $x/c = 0.42$, 0.50 , 0.60 , and 0.989 to compare with BANC data.

Figure 4.17 shows the wall pressure probes at the $0.989c$ position. For the 3D case, the figure shows that the fluctuations at the top and bottom surfaces are almost the same and in agreement with experiment. Also, shown in the figure the corresponding 2D results, which shows a difference in level between the SS and PS. This explains why in 2D there is an effect of tripping on the noise, which is absent for the 3D case.

4.3.3 Trailing-Edge and the Wake Flow

Figure 4.19 focuses on the dilatation field in the near wake just after the TE. The 3D data appears to show very fine coherent structures, and smaller amplitude waves. The TE noise discernable in the 3D data appear similar in the two cases, which will be discussed in greater detail in the following sections. In 2D the subsequent vortex-shedding (VS) of the TBL into the near wake for the tripped case appears to be more quiescent, i.e. the vortices are tighter, and more symmetric indicating less strength which leads to weaker VS noise. There also appears to be less dilatation (+/-) in the region just above and below the TE. This data is consistent with Figure 4.5 of the z -vorticity. The data thus shows two separate mechanisms; the vortex shedding mechanism, which is observed only for the 2D case. And, the TBL-TE scattering mechanism, which is observed in the realistic 3D simulations shown here.

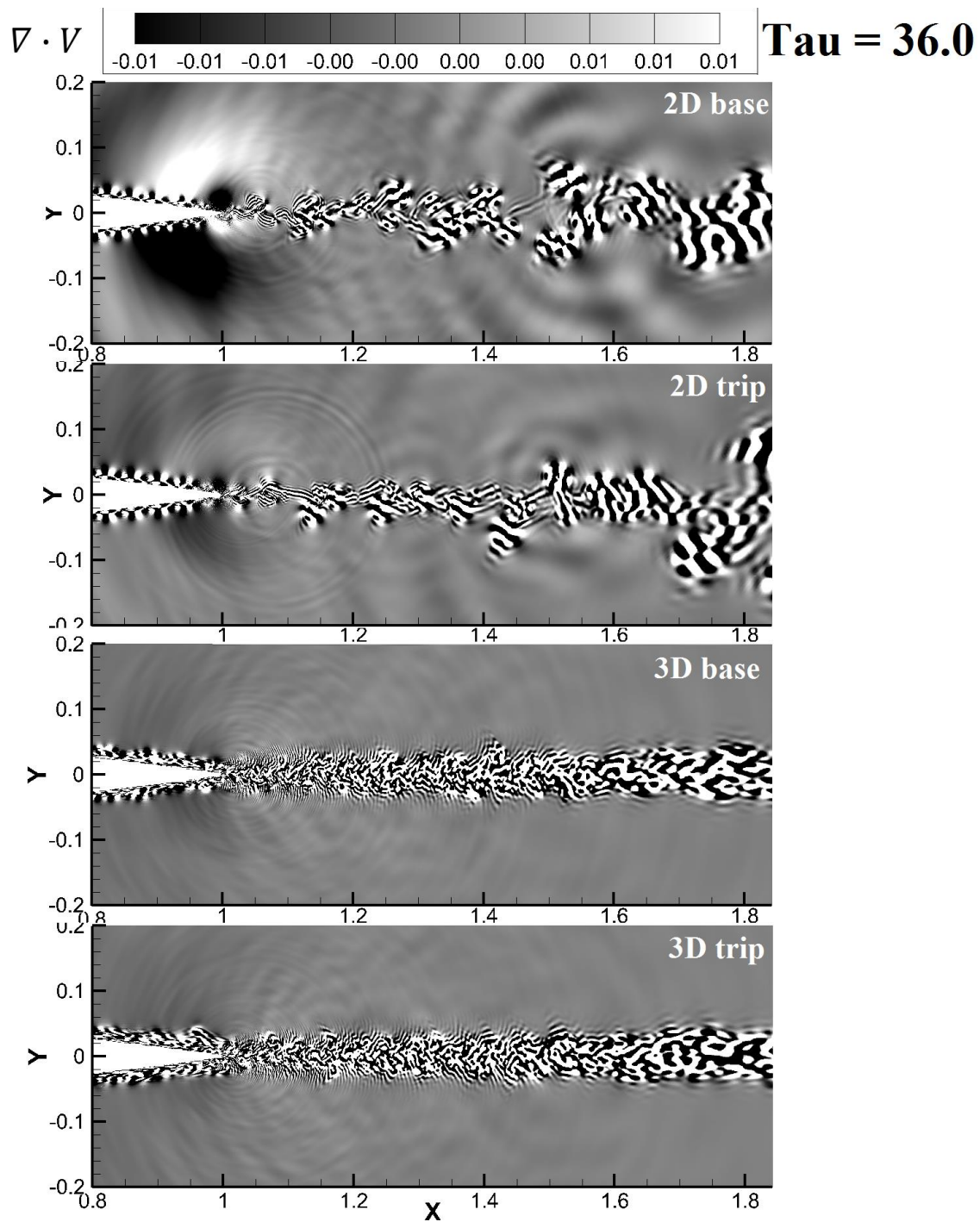


Figure 4.19 Instantaneous dilatation field plots at $\tau = 36$ for 2D (top two) and 3D (bottom two) Baseline (first, third) and trip 0.41c (second, fourth) cases, respectively.

The 3D instantaneous pressure field is shown in Figure 4.20. For the 3D case, the vortex shedding is not present at this level. For the 2D case we note vortex shedding that is weakened by the introduction of tripping. A close-up of what is happening in the pressure near the TE is shown in Figure 4.20:

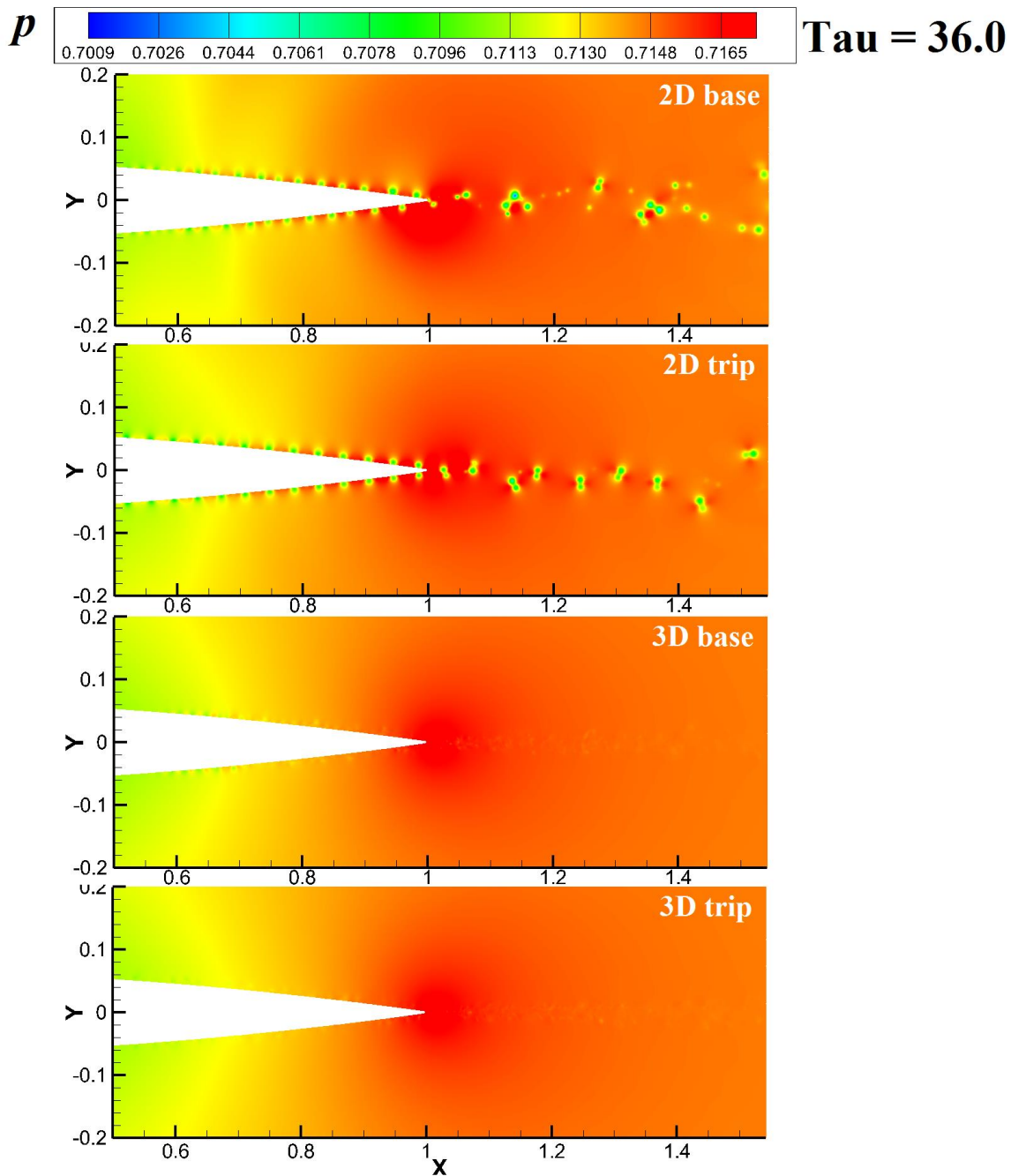


Figure 4.20 Instantaneous pressure field plots at tau = 36 for 2D (top two) and 3D (bottom two) Baseline (first, third) and trip 0.41c (second, fourth) cases, respectively.

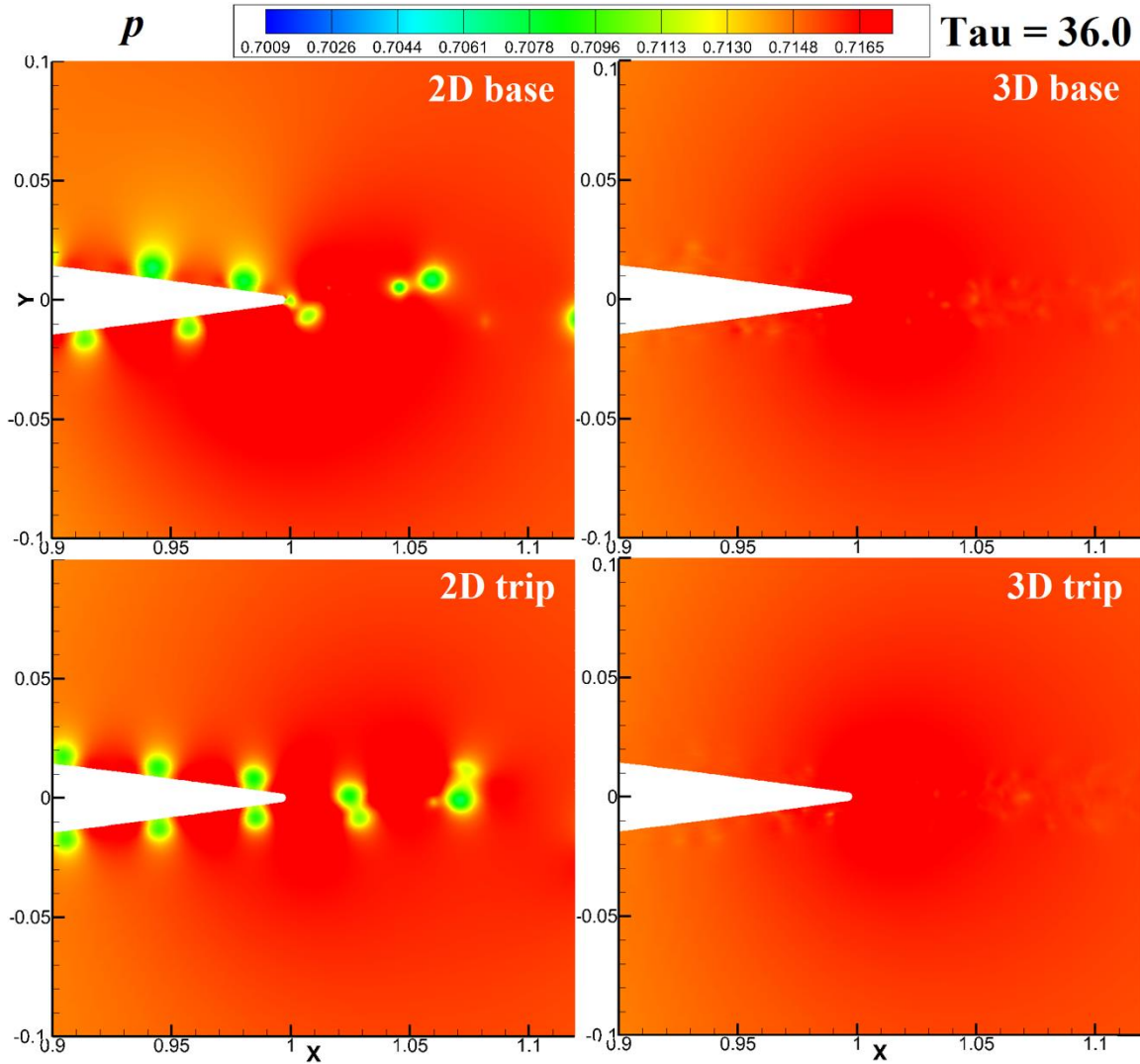


Figure 4.21 Instantaneous pressure field at $\tau = 36$ for 2D (left), and 3D (right) plots for the Baseline (top) and trip 0.41c (bottom) cases, respectively.

The fluctuating components of the pressure were taken aft the TE and in the region of the near wake to attempt to quantify if the pressure fluctuations are related to the vortex shedding, and its component of trailing-edge noise. In the following region of the near wake, Figure 4.22, the pressure, the divergence of velocity, and the vorticity were measured over a period of 1,024-time steps to be analyzed:

and PS as it convects past the TE, and of similar magnitude then the resulting condition when the two mixes in the near wake show much less fluctuations, perhaps indicating much less noise generated in the near wake as the corresponding SS and PS TBLs collide at the TE.

We next examine the wake vorticity field. The turbulence convected in the mean flow over the TE and generated in the near wake by the collision of the TBL of the PS and SS at the TE is directly relatable to the aeroacoustics noise generated in the field (Howe, 1988). Figure 4.24 is essential to this study as it gives us a snap-shot that shows how the vorticity within the TBLs interact at the TE. The 3D data in Figure 4.23 show very small structures of turbulence on the airfoil surface and in the near wake. In Figure 4.24 for 2D it appears by artificially tripping the BL symmetrically on SS and PS, the TBL profiles appear more symmetric, and in phase. With respect to the vorticity in the near wake, the tripped case appears similar in magnitude and more diffuse. The vortex pairs appear tighter, and more symmetric with respect to the $y=0$ axis of symmetry. For the Baseline case, however, the vortex pairs appear to be behaving in a more chaotic fashion where they seem to roll up and push into, and away from the axis of symmetry. This qualitative analysis indicates more vorticity in the 2D Baseline case.

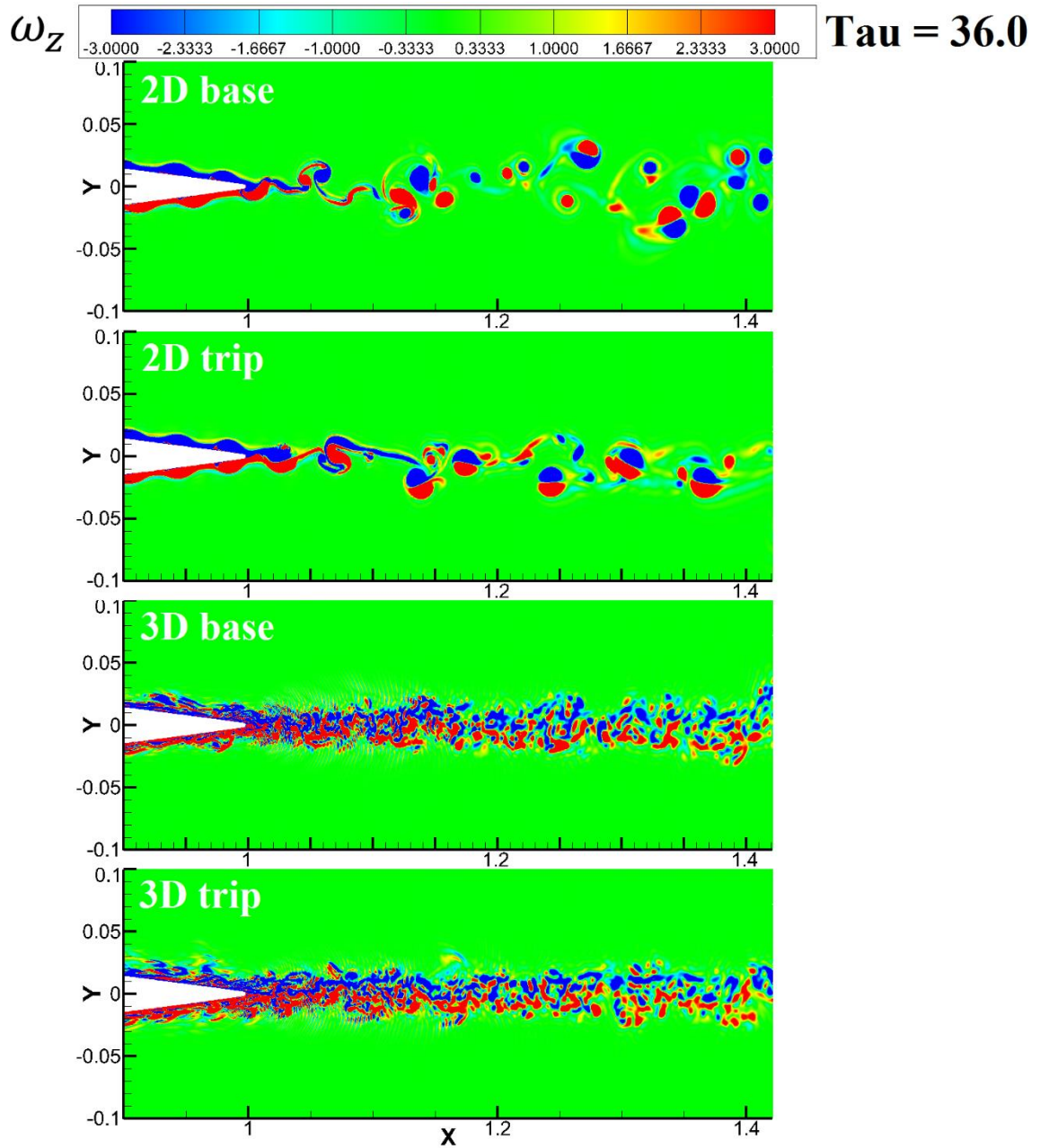


Figure 4.24 Instantaneous z-vorticity field plots at $\tau = 36$ for 2D (top two) and 3D (bottom two) Baseline (first, third) and trip 0.41c (second, fourth) cases, respectively.

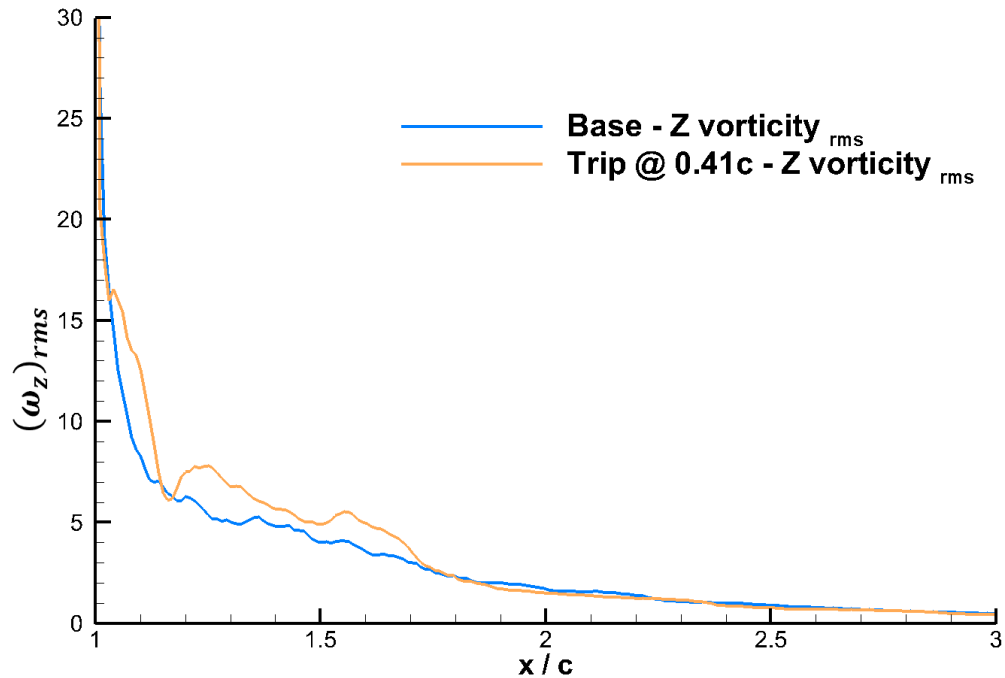


Figure 4.25 The RMS of vorticity was measured from $1 < x/c < 3$ within the near wake for 1,024-time steps to quantify the average vorticity fluctuations.

To further analyze the vorticity, data was recorded in the near wake for 1,024-time steps, performing an RMS to attempt to determine vortical fluctuations in the near wake, Figure 4.25. The figure shows that tripping slightly increases the vorticity in the wake. Figure 4.26 shows the RMS vorticity as function of y/c , and x/c , between the baseline (left), and tripped (right) cases:

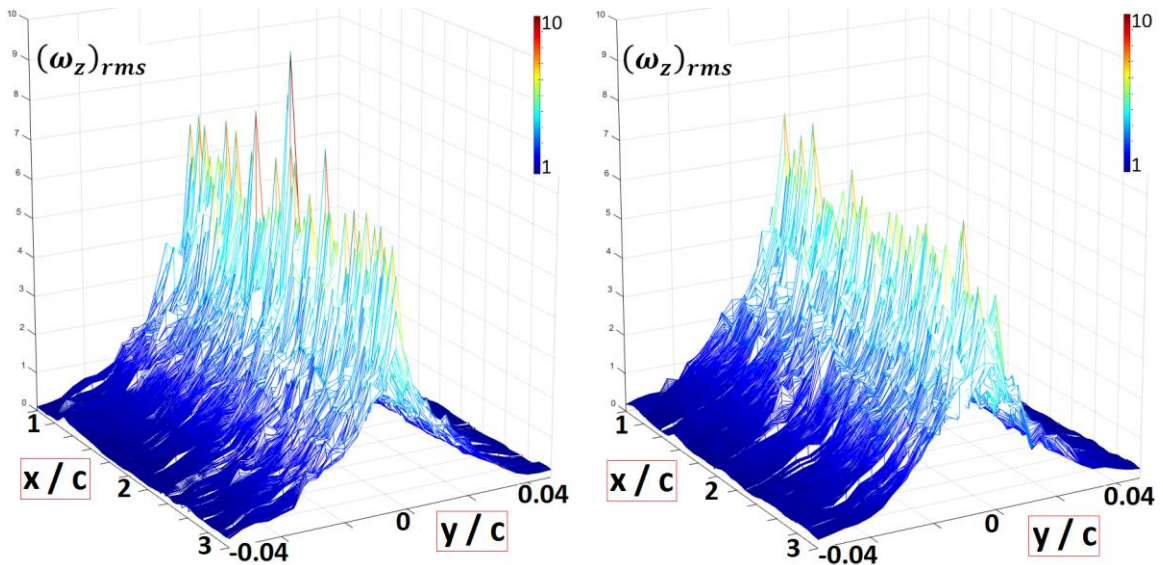


Figure 4.26 3D vorticity data extracted ($1 < x/c < 3$, $-0.04 < y/c < 0.04$) for 1,024-time steps, and RMS to see where the peak vorticity fluctuations occur.

To further illustrate where exactly the peak fluctuations are happening in the y -plane, Figure 4.27 is a 2D view looking upstream into the flow showing the vorticity over the length $-0.04 < y/c < 0.04$ identifying the RMS of vorticity within the given plane to give a better feel of the vorticity that exists in the near wake:

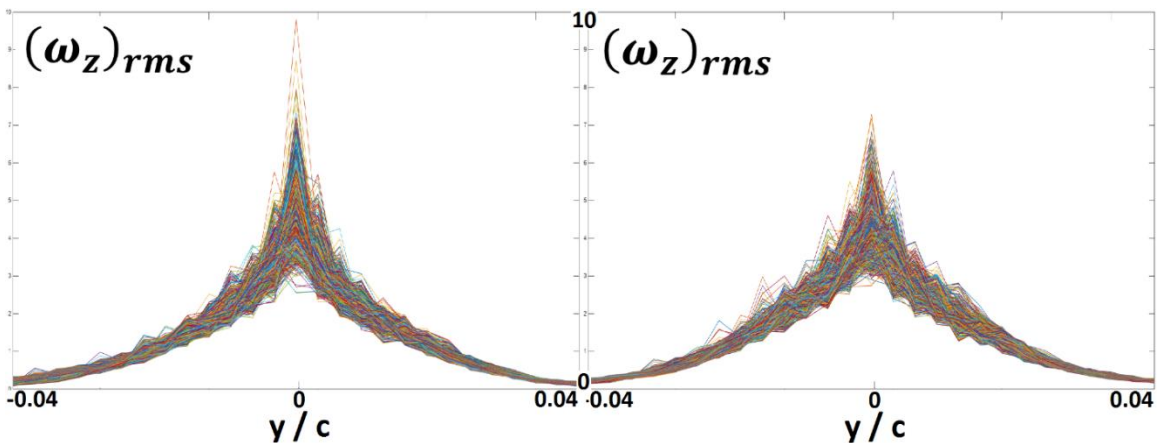


Figure 4.27 3D vorticity data extracted ($-0.04 < y/c < 0.04$) for 1,024-time steps, and RMS to see where the peak vorticity fluctuations occur.

It can be argued that although the RMS of vorticity patterns for the two cases are similar,

several features indicate the baseline case appears to have more vorticity in the near wake. Focusing on the $y = 0$ axis of symmetry, clearly the baseline case has more occurrences of higher peaks in this region. It could also be argued that for the baseline case the peaks are more tightly centered about the axis, whereas the tripped case tends to have more dispersed vorticity RMS as you move away from the axis of symmetry. This confirms and is consistent with the observation in Figure 4.23 that appears to show a more symmetric, and balanced dynamic behavior of the wake vorticity, indicative of less vorticity in the near wake for the tripped case.

4.4 The Acoustic Field

To further analyze the acoustic field about the airfoil TE, the BANC Workshop defined directivity patterns were explored with and without normalization, and are presented in Figures 4.28, and 4.29: This far-field data was taken at $2.5c$ above, and below the TE (refer to Figure 3.11). The directivity in Figure 4.29 do appear to compare reasonably with BANC data.

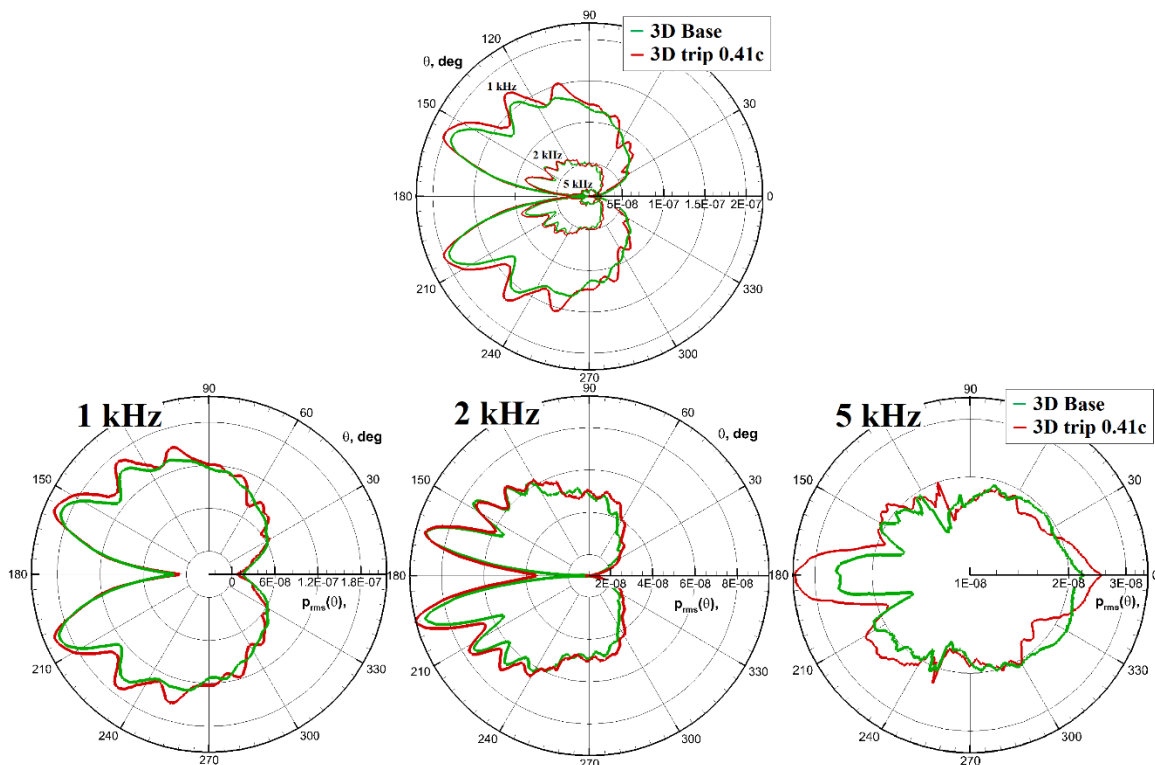


Figure 4.28 Non-normalized far field noise directivity patterns, $p_{rms}(\theta)$, same scale (top), relative scale (bottom) for 1 kHz band (left), 2 kHz (middle), and 5 kHz (right).

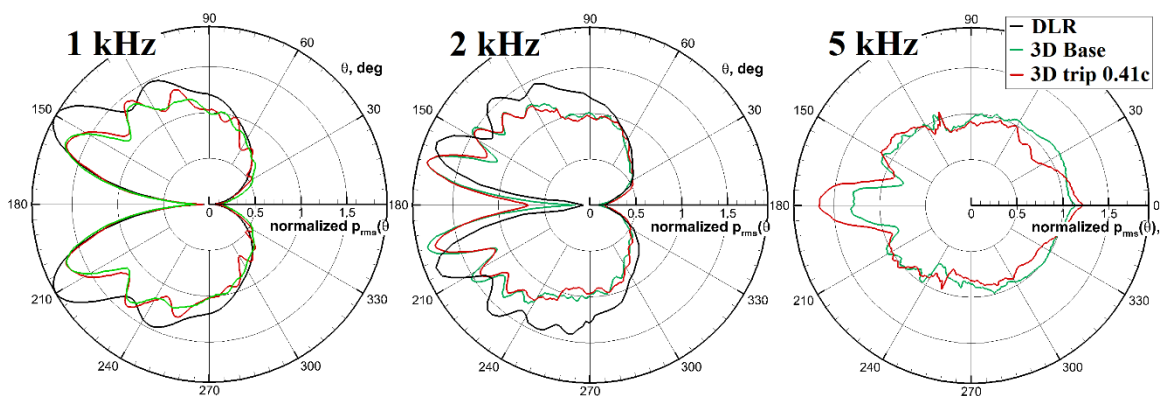


Figure 4.29 Normalized 3D far field 1/3-octave band noise directivity patterns as specified by the BANC workshop for 1 kHz band (left), 2 kHz (middle), and 5 kHz (right), with DLR data (Herr, 2015).

Table 4.2 Normalization values per case for Figure 4.27.

		Directivity pattern normalization value, $p_{rms}(\theta) * 10^{-6}$		
		1 kHz	2 kHz	5 kHz
2D	Baseline	1.9348	1.0595	0.0129
	trip 0.41c	1.1361	0.2299	0.0103
3D	Baseline	0.0926	0.0490	0.0157
	trip 0.41c	0.1070	0.0465	0.0207

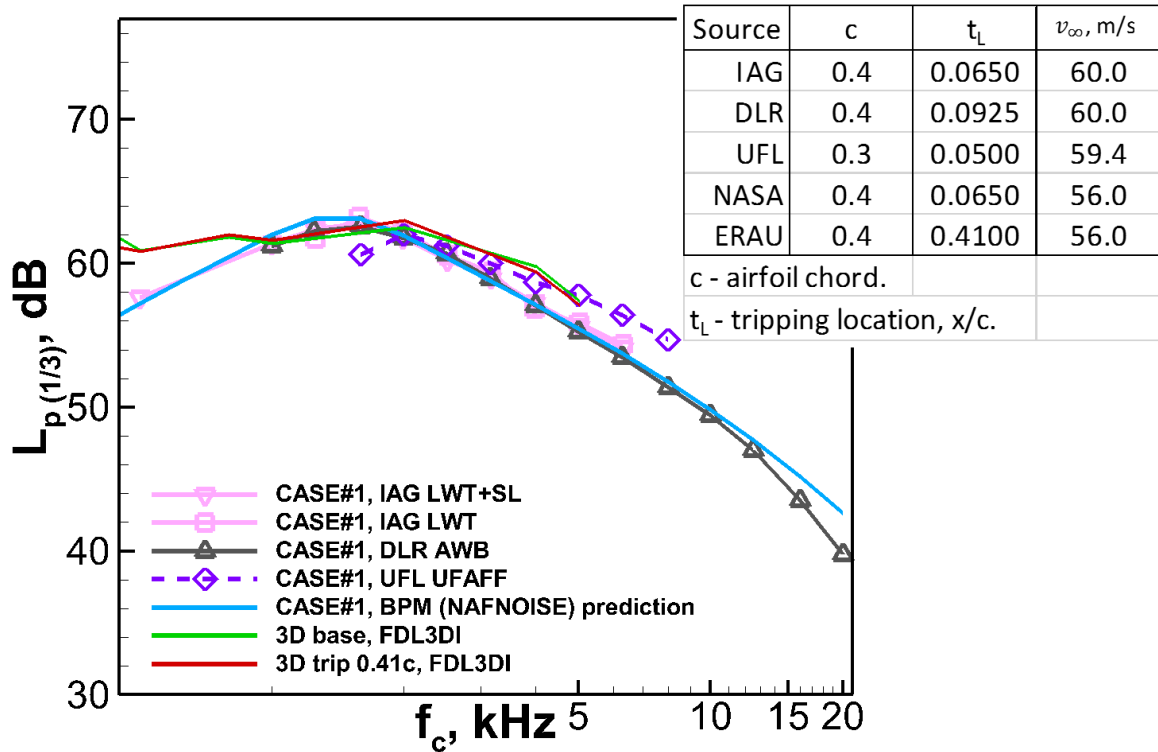


Figure 4.30 Far field one-third octave band for the baseline, and trip 0.41c cases at 2.5c above and below the TE with comparison data.

The spectra are shown in Figure 4.30. The 3D agrees with experiment and shows no tripping effect. The 2D spectra presented earlier are higher than the experiment and shows a strong tripping effect.

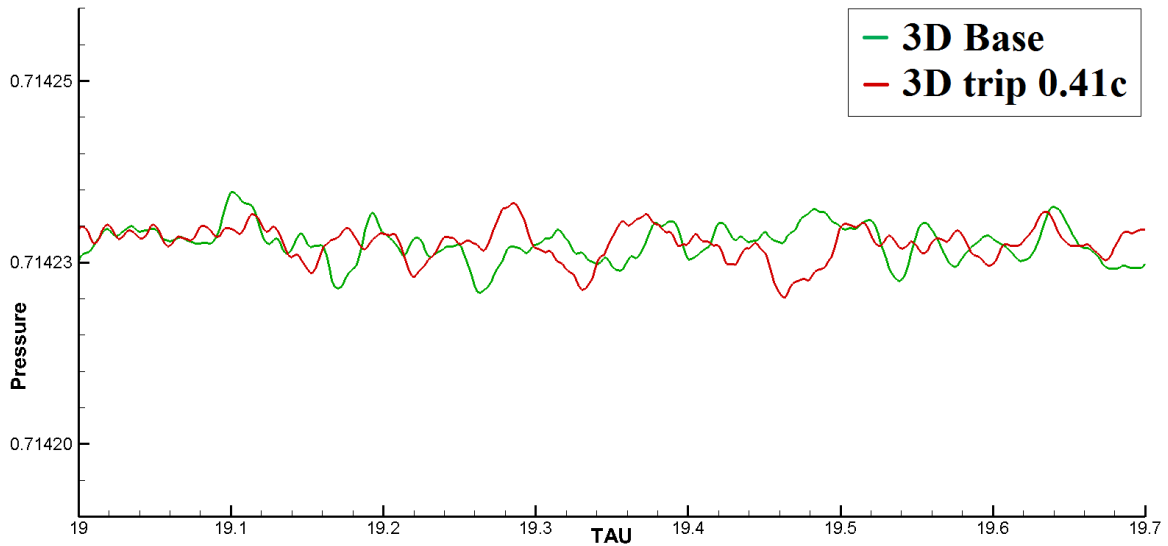


Figure 4.31 3D pressure time history for pressure probe located at station $(x, y) = (1, 2.5)$ for duration non-dimensional time $\text{Tau} = 19$ to 19.7 .

A comparison of the time trace of the pressure signals was investigated. For the far field pressure signal trace, Figure 4.31, it is apparent in the pressure time histories distinguishable features between 2D presented in Figure 3.14, and the 3D data. It is also observed that the amplitudes of the 3D data for both cases appear similar in magnitude, which would indicate similar noise levels. All of this is consistent with the far field spectra presented in Figure 4.30.

Further analysis commenced probing four more locations about the airfoil the BANC workshop far-field coordinate system with $r = 1m$ considering the $\alpha = 0^\circ$ chord-line with respect to the TE as being the $\theta = 0^\circ$ datum for the far field sweep, and moving counter-clockwise in ascending order, probe 1 was positioned at $\theta = 5^\circ$, probe 2 at $\theta = 120^\circ$, probe 3 at $\theta = 240^\circ$, and probe 4 at $\theta = 355^\circ$. This was an attempt to ascertain whether tripping affected noise in other directions other than $\theta = 90^\circ$, or was independent of θ . The specific angles selected were carefully chosen based on observations

in the directivity patterns. However, it was quickly ascertained that the very small magnitude of P_{rms} would not necessarily correspond with a significant difference in decibel. Figure 4.33 shows that tripping tends to slightly increase the noise at high frequencies. However, as is evident, the additional far-field study further confirms with its resulting spectra the tripping has minimal effect in a 3D sense.

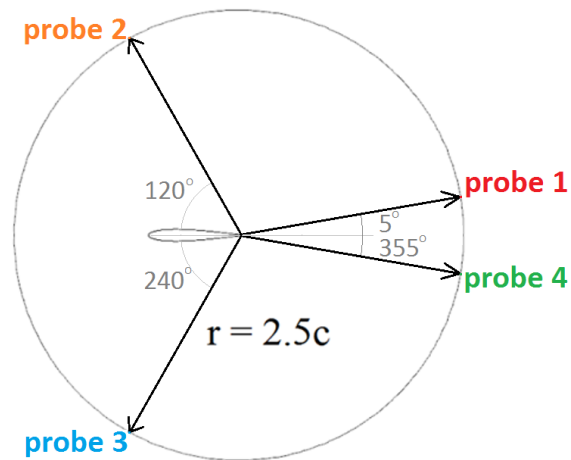


Figure 4.32 Far field data extraction location for further probing.

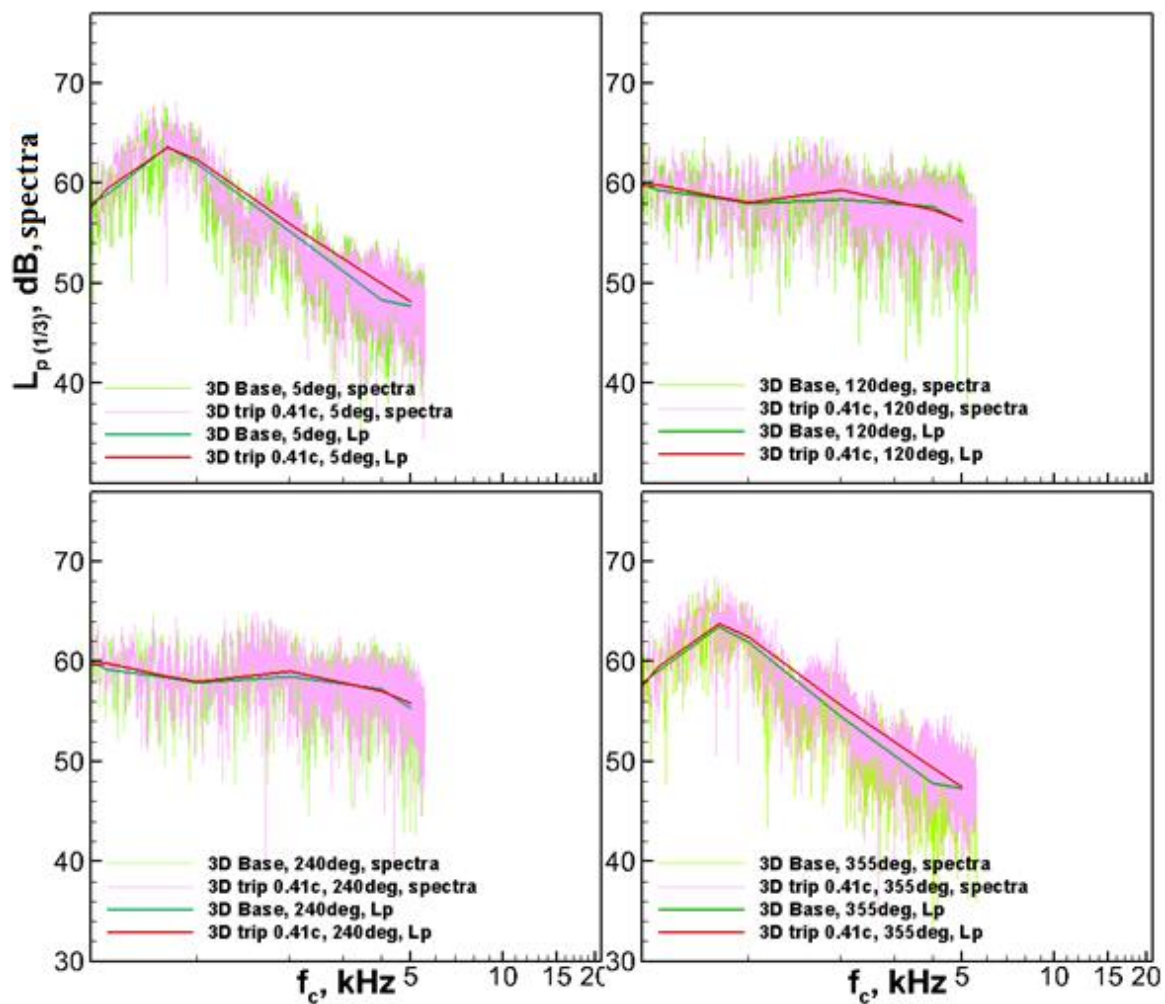


Figure 4.33 1/3-octave band far field noise with spectra, at $r = 1\text{m}$, $\theta = 5$ deg. (top left), $\theta = 120$ deg. (top right), $\theta = 240$ deg. (bottom left), and $\theta = 355$ deg. (bottom right), respectively.

5. Conclusions

Large-Eddy Simulations were presented herein to study the acoustic field associated with a NACA0012 airfoil for the tripped and untripped cases. Initially we have conducted quick 2D simulations to examine the effect of tripping on the radiated sound. The 2D studies have shown that tripping at x/c 0.41 reduces the radiated sound. Therefore, we presented herein 3D ILES for the clean (untripped) case and the tripped at x/c 0.41 case.

In the 2D simulations considered here, vortex shedding seems to play a key role in sound generation for the untripped case. When the flow is tripped identically on both the upper and lower surfaces, the transition process was identical in both sides leading to diminishing the vortex shedding, e.g. Figure 4.18 and 4.23, and the radiated sound in Figure 4. 28. This mechanism however, seems not to be present in the results of the subsequent, realistic 3D simulations.

The following conclusions pertain to the 3D simulations:

A: The Flow near the Airfoil:

1. The predicted boundary layer growth and turbulence intensity agreed with the experimental results (Figure 4.13).
2. Examining the surface pressure and velocity and pressure fluctuations shows that tripping moves upstream and localizes the transition onset. The peak fluctuations for the tripped case is higher than that of the clean case. But, the level of flow fluctuations by the trailing edge is practically the same for the tripped and untripped cases. (Figure 4.10).
3. Fluctuating pressure along the centerline of the near wake is reduced

because of tripping. As for the vorticity in the near wake, tripping seems to slightly broaden its extent in the direction perpendicular to the flow. (Figure 4.22, and 4.27).

B) The Acoustic field:

1. Snap shots of the acoustic pressure and dilation fields seems to indicate that the code is capable of directly predicted the radiated sound with no boundary reflections within the computational domain (Figure 4.2, and 4.3).

2. The predicted far field sound spectra and directivity are in close agreement with the BANC data although the span-wise width for the present simulations is smaller than that of the experiment (Figures 4.29, and 4.30).

3. Tripping, while it does introduce localized disturbances near the trip location, the fluctuations near the trailing edge is independent of tripping, as pointed out earlier. The radiated sound is found to be independent of tripping. This may lead us to believe that in this case, the dominant sound source is the scattering of the flow fluctuations near the trailing edge. (Figure 4.11).

4. Tripping slightly increased the radiated sound at high frequencies (5 kHz), however, this should be taken with caution as this close to the cut-off of the resolved scales limit. (Table 4.2).

Overall the results seem to be encouraging that this LES code can be used for further studies focusing on suppressing of airframe noise.

REFERENCES

- Abbott, I.A., Von Doenhoff, A.E., (1959). *Theory of Wing Sections*. Dover Publications, Inc. New York, NY.
- Archibald, F.S., (1975). The Laminar BL Instability Excitation of an Acoustic Resonance. *J. Sound and Vibration*, (1975) 38(3), 387-402.
- BANC collaborative website, (2016). URL: https://info.aiaa.org/tac/ASG/FDTC/DG/BECAN_files/ [cited April 11, 2017].
- Bahr, C., Li, J., and Cattafesta, L., (2011). “Aeroacoustics Measurements in Open-Jet Wind Tunnels – An Evaluation of Methods Applied to Trailing-Edge Noise”, *AIAA Paper 2011-2771*.
- Brooks, T.F., Hodgson, T.H., (1981). “Trailing Edge Noise prediction from Measured Surface Pressures”, *Journal of Sound and Vibration*, 69-117.
- Brooks, T.F., Pope, D.S., Marcolini, M.A., (1989). “Airfoil Self-Noise and Prediction”, *NASA RP-1218*, 1-137.
- Casper, J., Farasat, F., (2004). “Broadband TEN predictions in the time domain”, *J. Sound and Vibration*, 271 (2004) 159-176.
- Chaitanya, P., (2015). “Aerofoil geometry effects on turbulence interaction noise”, *AIAA Paper 2015-2830*.
- Delfs, Ing. Jan, (2009). “Grundlagen der Aeroakustik”, Lecture notes at Technische Universität Braunschweig, Braunschweig, Germany.
- Dobrzynski, W., (2010). “Almost 40 years of Airframe Noise Research. What did we achieve?” *J. Aircraft*, Vol. 47, No. 2.

- Drela, M., (2014). *Flight Vehicle Aerodynamics*. The MIT Press, Cambridge, MA.
- Engineering Toolbox Website, (2017). URL: <http://www.engineeringtoolbox.com/> [cited April 13, 2017].
- Gaitonde, D.V., Visbal, M.R., (1999). "Further development of a Navier-Stokes Solution Procedure Based on High-Order Formulas", *AIAA Paper 1999-0557*.
- Garrec, T.L., Gloerfelt, X., (2008). "Direct noise computation of TEN at high Reynolds numbers", *AIAA Paper 2008-2914*.
- Garmann, D., (2012). "Comparative study of implicit and subgrid-scale model large-eddy simulation techniques for low-Reynolds number airfoil applications", *Int. J. Numerical Methods Fluids 71:1546-1565*.
- Georgiadis, N. J., Rizzetta, D. P., Fureby, C., (2010). "Large-Eddy Simulation: Current Capabilities, Recommended Practices, and Future Research," *AIAA Journal, Vol. 48, No. 8*.
- Golubev, V.V., Nguyen, L., Roger, M. and Visbal, M.R., (2011). "On Interaction of Airfoil Leading and Trailing Edge Noise Sources in Turbulent Flow", *AIAA Paper 2011-2859*.
- Golubev, V.V., Nguyen, L., Roger, M., and Visbal, M.R., (2012). "High-Accuracy Simulations of Flow-Acoustics Resonant Interactions in Airfoil Transitional Boundary Layers", *AIAA Paper 2012-2136*.
- Golubev, V.V., Nguyen, L.D., Mankbadi, R.R., Roger, M., Dudley, J.G., Visbal, M.R., (2013). "On Self-Sustained Flow-Acoustic Resonant Interactions in Airfoil Transitional Boundary Layers", *AIAA Paper 2013-2619*.

- Herr, M., Ewert, R., Rautmann, C., (2015). “Broadband Trailing-Edge Noise Predictions- Overview of BANC-III Results”, *AIAA Paper 2015-2847*, 2015.
- Herrig, A., Wurz, W., Kramer, E., Wagner, S., (2008). “New CPV-Results of NACA 0012 Trailing-Edge Noise”, *International Conference on Methods of Aerophysical Research, ICMAR*.
- Howe, M.S., (1988). “The Influence of Surface Rounding on Trailing Edge Noise”, *J. of Sound and Vibration 126(3)*, 503-523.
- Lele, Sanjiva K. (1992). “Compact Finite Difference Schemes with Spectral-like Resolution.” *Journal of Computational Physics* 103 (1). Elsevier: 16–42.
- Lilley, G.M., (1998). “A Study of the Silent Flight of the Owl”, *AIAA Paper 1998-2340*.
- Lowson, M.V., Fiddes, S.P., Nash, E.C., (1994). “Laminar Boundary Layer Aeroacoustics Instabilities”, *AIAA Paper 94-0358*.
- Mankbadi, R.R., (1994). *Transition, Turbulence, and Noise: Theory and Applications for Scientists and Engineers*. Kluwer Academic Publishers, Norwell, Massachusetts, USA.
- Mankbadi, R., Golubev, V., Sansone, M., Sewell, C., and Nguyen, L., (2015). “Effect of a Synthetic Jet Actuator on Airfoil Trailing Edge Noise”, *Int. J. of Aeroacoustics, Vol. 14, No. 3&4, 2015*.
- Mankbadi, R., Lo, S.-C., Lyrintzis, A.S., Golubev, V., Dewan, Y., and Kurbatskii, (2016). “Hybrid LES-RANS Simulations of Jet Impinging on a Flat Plate”, *Journal of Acoustics, April 7, 2016, doi: 10.1177/1475472X16642355*.
- Mankbadi, R., (2001). “Computational Aeroacoustics, in “New Trends in Turbulence”, (Ed. M. Lesieur), Springer-Verlag Berlin Heidelberg.

- Nguyen, L.D., (2016). “Tonal Noise Generation by Moderate Reynolds Number Airfoils”, PhD Dissertation, Embry-Riddle Aeronautical University, Daytona Beach, FL.
- Oerlemans, S., Sijtsma, P., Mendez Lopez, B., (2007). “Location and quantification of noise sources on a wind turbine”, *J. Sound and Vibration*, 299 (2007) 869-883.
- Olshausen, B.A., (2000). “Aliasing”, Lecture notes at Berkeley, Oakland, CA.
- Paterson, R., Vogt, P., Fink, M. and Munch, C., (1973). “Vortex Noise of Isolated Airfoils.” *J. Aircraft*. 10 (1973) 296-302.
- Sagrado, A.G., Hynes, T., Hodson, H., (2006). “Experimental Investigation into Trailing Edge Noise Sources”, *AIAA Paper 2006-2476*.
- Sherer, Scott. (2003). “Further Analysis of High-Order Overset Grid Method with Applications”, *AIAA Paper 2003-3839*.
- Suhs, N.E., Rogers, S.E., Dietz, W.E., (2002). “Pegasus 5: An Automated Pre-Processor for Overset-Grid CFD”, *AIAA Paper 2002-3186*.
- Swales, C., Lawson, M.V., (1997). “Aero-acoustic study on a NACA 0012 aerofoil”, *AIAA Paper, AIAA-97-0509*.
- Tam, C., (2012). *Computational Aeroacoustics: A Wave Number Approach*. Cambridge University Press, New York, NY.
- Visbal, M.R., Gaitonde, D.V., (1998). “High-Order Schemes for Navier-Stokes Equations: Algorithm and Implementation into FDL3DI,” *AFRL-VA-WP-TR-1998-3060*, Wright-Patterson Air Force Base, Ohio 45433-7913.
- Visbal, M. R., and Gaitonde, D. V., (2002). “On the use of High-Order Finite-Difference Schemes on Curvilinear and Deforming Meshes,” *Journal of Computational Physics, Vol. 181, pp.155–185*.

Winkler, J., Moreau, S., Carolus, T., (2009). “Large Eddy Simulation and Trailing-Edge Noise Prediction of an Airfoil with Boundary-Layer Tripping”, *AIAA Paper*, *AIAA-2009-3197*.